Dynamics of magma mixing and magma mobilisation beneath Mauna Loa – insights from the 1950 southwest rift zone eruption

Maren Kahl[1,*], Daniel J. Morgan[2], Carl Thornber[3], Richard Walshaw[2], Kendra J. Lynn[4], Frank A. Trusdell[4]

Supplementary Material

1. Analytical methods

1.1 Electron microprobe analysis

Mineral and glass microanalysis were performed using a JEOL JXA8230 electron probe microanalyzer at the University of Leeds Microscopy and Spectroscopy Centre (LEMAS), a JEOL 8230 SuperProbe electron probe microanalyzer at the Institute of Earth Sciences, University of Iceland, a JEOL8900 electron probe microanalyzer at the USGS Denver Microbeam Facility, and a JEOL SuperProbe JXA-iSP100 electron probe microanalyzer at the Institute of Earth Sciences, Heidelberg University. The following run conditions were used:

Olivine and pyroxene: Backscattered electron (BSE) images and quantitative concentration profiles (spacing ~4-7µm) of major and minor elements (olivine: Si, Fe, Mg, Mn, Ca, Ni, Cr; clinopyroxene and orthopyroxene: Si, Fe, Mg, Ca, Al, Na, Ti, Mn, Cr) in a total of 183 olivine and 37 pyroxene (clinopyroxene: 6; orthopyroxene: 31) crystals were obtained using a JEOL JXA8230 electron microprobe analyser at the University of Leeds Microscopy and Spectroscopy Centre (LEMAS). Accelerating voltage of 15kV, 30nA beam current, and fully-focussed spot size for olivine and pyroxene analysis were used. A list of primary standards used for calibration including peak and background count times for olivine and pyroxene are summarized in table 1. Internal data reduction for olivine and pyroxene analysis was performed using the Phi-Rho-Z matrix correction algorithm of Armstrong/Love Scott implemented within

the PFE software package (Donovan et al. 2012) and the Jeol implementation by Paul Carpenter (version 3.50) of the CITZAF (Armstrong 1993) quantitative correction program. Total oxides for olivine and pyroxene range between 98.2 and 103.1 with a mean value of 100.5±0.7 (1σ) for olivine and 99.9±0.8 (1σ) for pyroxene. Precision was assessed using EPMA software-calculated 1 sigma count statistic errors (Wieser et al. 2022). Relative analytical precision for olivine is on average <1% for Si, Mg and Fe; ~2.8% for Ca; ~8.8% for Ni and Mn (see Supplementary Data table S2). Accuracy based on repeat analysis of GEO2 MKII olivine standard is on average: ±1.1% for Si; ±0.4% for Mg; ±5.2% for Fe and ±7.9% for Ni. Elements with low abundance in GEO2 MKII olivine return low accuracy (±26%; see table S2). Relative analytical precision for pyroxene is on average <1% for Si, Fe and Ca; 2.1% for Al; ~4% for Ti and Mg; ~7% for Mn and Cr (see Supplementary Data table S3). Accuracy based on repeat analysis of GEO2 MKII diopside standard is: <1% for Si, Ca and Mg; ±10.8% for Fe (see table S3).

Spinel: Single spot analysis (n=181) of Ti, Al, Fe, Mn, Mg, Cr and Ni in a total of 40 spinels were performed using a JEOL 8230 SuperProbe electron microprobe analyser at the Institute of Earth Sciences, University of Iceland. Run conditions were 15keV, 20nA, and a focused beam diameter. A list of primary standards used for calibration including peak and background count times for oxide analysis are included in table 1. Internal data reduction for all spinel analysis was performed using the ZAF correction. Total oxides for spinel range between 96.7 and 100.8, averaging around 99.1±0.7 (1σ). Precision was assessed using EPMA software-calculated 1 sigma count statistic errors. Relative analytical precision for spinel is <1% for Al, Fe, Mg and Cr; 1.7 % for Ti; ~8% for Ni and 14.3 % for Si (see Supplementary Data table S5).

Plagioclase: Single spot analysis (n= 175) of major and minor elements (Na, Mg, Al, Si, K, Ca, Fe, Sr and Ba) in a total of 20 plagioclase crystals were performed using the *JEOL* SuperProbe JXA-iSP100 electron probe microanalyzer at the Institute of Earth Sciences,

Heidelberg University. Run conditions were 15keV, 10nA, and spot size of 10µm. A list of primary standards used for calibration including peak and background count times for plagioclase analysis are included in table 1. Internal data reduction for all plagioclase analyses was performed using the Phi-Rho-Z matrix correction algorithm of Armstrong/Love Scott (Armstrong 1988). Total oxides for plagioclase range between 99.6 and 101.7, averaging around 100.6±0.4 (1σ). Precision was assessed using EPMA software-calculated 1 sigma count statistic errors. Relative analytical precision is <1% for Si, Al, Ca; 1.6% for Na; 2.6% for Mg; 3.4% for Fe, and 8.9% for K (see Supplementary Data table S4). Accuracy was monitored by measuring the following secondary standard during each session: Plagioclase (Anorthite) from Great Sitkin Island, Alaska (NMNH137041). Accuracy is: ±0.1% and ±0.5% for Al and Si; ±2.9% and ±3.1% for Ca and Na. Elements with low abundance in NMNH137041 return low accuracy (±25% or greater; see table S4).

Groundmass glass: Single spot analysis (n=422) of Si, Ti, Al, Fe, Mn, Mg, Ca, Na, K, Cr, P, S in 45 groundmass glass were performed using a JEOL8900 electron probe microanalyzer at the USGS Denver Microbeam Facility by C. Thornber. Groundmass glasses were analysed using an accelerating voltage of 15keV, 20nA beam current, and 10-20 µm spot size (similar to methods previously reported in Thornber et al. 2002, 2001). A list of primary standards used for calibration including peak and background count times for glass analysis are included table 1. Matrix corrections were performed using a Phi-Rho-Z routine for internal data reduction of all glass analysis. Precisions were estimated by measuring secondary standard basalt glass VG-A99 (USNM 113498-1; Makaopuhi Lava Lake; Jarosewich 2002). Major (>1 wt%) and minor (<1wt%) glass contents were determined with precisions better than 1σ = 4.7% and 11.9%. Accuracy is: ±0.7 and ±0.1% for Mg and Al; ±1.4, ±1.6, ±1.7 and ±1.7 for Ca, Ti, Si and Fe; ±2.1 and ±2.5 for K and Na (see table S7).

Melt inclusions: Single spot analysis (n=28) of major and minor elements (Si, Ti, Al, Fe, Mn, Mg, Ca, Na, K, Cr, P) in 20 olivine-hosted, glassy melt inclusions were performed using a JEOL 8230 SuperProbe electron microprobe analyser at the Institute of Earth Sciences, University of Iceland. An accelerating voltage of 15keV, 10nA beam current, and 10µm spot size. Smaller melt inclusions have been measured with a spot size of 5µm. A list of primary standards used for calibration including peak and background count times for glass analysis are included table 1. The CITZAF correction program (Armstrong 1991) was used for internal data reduction of all glass analyses. Total oxides for melt inclusion glass range between 99.85 and 99.87, averaging around 99.86±0.01 (1σ). Precision was assessed using EPMA software-calculated 1 sigma count statistic errors. Relative analytical precision for major (>1 wt%) and minor (<1wt%) glass contents is better 2.4% and 13.5%. Accuracy based on repeat analysis of VG-A99 basalt glass standard (USNM 113498-1; from Makaopuhi Lava Lake; Jarosewich 2002) is: ±0.3% for Si; ±1.1% for K and Al; ±1.4%, ±1.6% and ±1.7% for Mg, Ca and Fe; ±2.5% and ±2.8% for Ti and Na (see table S8).

Table 1: List of primary standards, spectrometers, analytical crystals, peak and background count times and detection limits (DLs)

	Element	Spec.	Crystal	Standard	Peak (sec)	Backgr. (sec)	DLs (ppm)
Pyroxene (Probe for EPMA Interface)	Si	5	TAP	Geo2 Diopside 7308 (natural; Dog Lake, Ontario, Canada)	20	10	80
	Ti	2	LIFL	Geo2 Rutile 7320 (synthetic)	20	10	240
	Al	5	TAPH	Geo2 Kyanite 7315 (natural; Collinsville, CT, USA) or Geo2 Kspar 7314 (natural; Lucerne, Switzerland)	20	10	80
	Fe	4	LIFH	Geo2 Fe2O3 (natural; Bouse, La Paz Co, Arizona, USA)	20	10	200
	Mn	4	LIFH	Geo2 Rhodonite 7319 (natural; Broken Hill, NSW, Australia)	20	10	180
	Mg	3	TAPH	Geo2 Diopside 7308 (natural; Dog Lake, Ontario, Canada)	20	10	100
	Ca	1	PETJ	Geo2 Diopside 7308 (natural; Dog Lake, Ontario, Canada)	20	10	140
	Na	3	TAPH	Geo 2Jadeite 7313 (natural; Tawmaw, Myanmar)	20	10	110
	Cr	2	LIFL	Geo2 Cr2O3 7307 (synthetic)	20	10	230
Pyroxene (Jeol PC-EPMA Interface)	Si	1	TAP	Geo2 Diopside 7308 (natural; Dog Lake, Ontario, Canada)	15	7	170
	Ti	2	PETL	Geo2 Rutile 7320 (synthetic)	20	10	78
	Al	5	TAP	Geo2 Kyanite 7315 (natural; Collinsville, CT, USA)	20	10	70
	Fe	4	LIFH	Geo2 Fe2O3 (natural; Bouse, La Paz Co, Arizona, USA)	30	15	107
	Mn	4	LIFH	Geo2 Rhodonite 7319 (natural; Broken Hill, NSW, Australia)	30	15	106
	Mg	3	TAPH	Geo2 Diopside 7308 (natural; Dog Lake, Ontario, Canada)	20	10	64
	Ca	2	PETL	Geo2 Diopside 7308 (natural; Dog Lake, Ontario, Canada)	15	7	67
	Na	3	TAPH	Geo 2Jadeite 7313 (natural; Tawmaw, Myanmar)	15	7	99
	Cr	4	LIFH	Geo2 Cr2O3 7307 (synthetic)	20	10	124
Olivine (Probe for EPMA Interface)	Si	5	TAP	Geo2 Diopside 7308 (natural; Dog Lake, Ontario, Canada)	20	10	90
	Ti	2	LIFL	Geo2 Rutile 7320 (synthetic)	20	10	240
	Al	5	TAP	Geo2 Kyanite 7315 (natural; Collinsville, CT, USA)	20	10	90
	Fe	4	LIFH	Geo2 Fe2O3 (natural; Bouse, La Paz Co, Arizona, USA)	20	10	190
	Mn	4	LIFH	Geo2 Rhodonite 7319 (natural; Broken Hill, NSW, Australia)	20	10	170
	Mg	3	TAPH	Geo2 Diopside 7308 (natural; Dog Lake, Ontario, Canada)	20	10	100
	Ca	1	PETJ	Geo2 Diopside 7308 (natural; Dog Lake, Ontario, Canada)	20	10	130
	Cr	2	LIFL	Geo2 Cr2O3 7307 (synthetic)	20	10	220

	Ni	2	LIFL	Geo2 Ni metal 7317 (pure)	20	10	290
Olivine (Jeol PC-EPMA Interface)	Si	1	TAP	Geo2 Almandine 7302 (natural; Roxby, CT, USA)	40	20	130
	Ti	4	PETH	Geo2 Rutile 7320 (synthetic)	20	10	18
	Al	3	TAPH	Geo2 Kyanite 7315 (natural; Collinsville, CT, USA)	60	30	12
	Fe	2	LIFL	Springwater Meteorite Olivine (USNM 2566)	40	20	134
	Mn	2	LIFL	Geo2 Rhodonite 7319 (natural; Broken Hill, NSW, Australia)	60	30	163
	Mg	5	TAP	Springwater Meteorite Olivine (USNM 2566)	40	20	83
	Ca	4	PETH	Geo2 Diopside 7308 (natural; Dog Lake, Ontario, Canada)	20	10	40
	Cr	2	LIFL	Geo2 Cr2O3 7307 (synthetic)	20	10	160
	Ni	2	LIFL	Geo2 Ni metal 7317 (pure)	60	30	126
Plagioclase	Si	5	TAPL	Anorthite (NMNH 137041)	40	20	63
	Al	1	TAP	Anorthite (NMNH 137041)	40	20	109
	Fe	3	LIFL	Hematite (Natural Fe_2O_3; Geo2 Mk II, P&H Developments)	40	20	113
	Mg	5	TAPL	Augite (Kakanui) (NMNH 122142)	40	40	28
	Ca	4	PETL	Anorthite (NMNH 137041)	20	10	93
	Na	1	TAP	Jadeite (Natural $NaAlSi_2O_6$; Geo2 Mk II, P&H Developments)	30	15	108
	K	4	PETL	Orthoclase (Geo2 Mk II, P&H Developments)	40	20	53
	Ba	2	PETL	Baryte (Natural $BaSO_4$; Geo2 Mk II, P&H Developments)	40	40	84
	Sr	4	PETL	Celestite (Natural $SrSO_4$; Geo2 Mk II, P&H Developments)	40	40	145
Spinel	Si	1	TAP	Pyrope (NMNH 143968)	30	30	73
	Ti	2	PETJ	Rutile (Astimex Standards Ltd.)	30	30	151
	Al	1	TAP	Chromite (NMNH 117075)	30	15	58
	Fe	3	LIFH	Hematite (Astimex Standards Ltd.)	30	15	119
	Mn	4	LIFL	Bustamite (Astimex Standards Ltd.)	30	30	108
	Mg	5	TAP	Hypersthene (USNM 746)	30	30	41
	Cr	4	LIFL	Chromite (NMNH 117075)	30	15	117
	Ni	3	LIFH	Pentlandite (Astimex Standards Ltd.)	30	30	107

	Element	Spec.	Crystal	Standard	Peak (sec)	Backgr. (sec)	DLs (ppm)
Groundmass glass	Si	3	TAP	Tiburon Albite	20	10	n.a.
	Ti	4	PETJ	TiO_2 (synthetic)	20	10	n.a.
	Al	3	TAP	Miyake Anorthite	20	10	n.a.
	Fe	2	LIFH	Fayalite (synthetic)	20	10	n.a.
	Mn	2	LIFH	Spessartine	20	10	n.a.
	Mg	1	TAP	Springwater Meteorite Olivine (USNM 2566)	20	10	n.a.
	Ca	4	PETJ	Miyake Anorthite	20	10	n.a.
	Na	1	TAP	Tiburon Albite	20	10	n.a.
	K	4	PETJ	Or-1A Orthoclase	20	10	n.a.
	P	4	PETJ	Wilberforce Apatite	20	10	n.a.
	Cr	2	LIFH	$MgCrO_4$ (synthetic)	20	10	n.a.
	S	5	PETJ	Barite	80	40	n.a.
Melt inclusions	Si	1	TAP	Tectite Glass (NMNH 2231)	30	10	159
	Ti	2	PETJ	Hornblende (Kakanui) (NMNH 143965)	40	20	161
	Al	1	TAP	Anorthite (NMNH 137041)	30	15	107
	Fe	4	LIFL	Garnet (NMNH 87375)	40	20	164
	Mn	4	LIFL	Bustamite (Astimex Standards Ltd.)	40	20	145
	Mg	5	TAP	Diopside Glass (NASA)	30	15	91
	Ca	2	PETJ	Diopside Glass (NASA)	30	15	117
	Na	5	TAP	Omphacite (NMNH 110607)	20	10	137
	K	2	PETJ	Corning Glass D (NMNH 117218-3)	40	20	76
	P	2	PETJ	Apatite (Astimex Standards Ltd.)	40	20	139

n.a.: No detection limits available

1.2 Electron backscatter diffraction (EBSD)

Crystallographic orientations of olivine crystals were determined using electron backscatter diffraction (EBSD, Costa and Chakraborty 2004; Prior et al. 1999) on the FEI Quanta 650 FEGSEM at the University of Leeds Electron Microscopy and Spectroscopy Centre (LEMAS). Constraint of crystallographic directions in olivine with respect to the micro-analytical traverses is essential for accurate diffusion modelling (Costa and Chakraborty 2004), as the diffusivity of different elements (e.g. Fe-Mg or Ni) in olivine is strongly anisotropic, with diffusion along the c-axis six times faster than along the a- and b-axes (e.g. Dohmen et al. 2007a; Clark and Long 1971). To minimize uncertainty in the determination of the orientation data we applied the procedures outlined in Kahl et al. (2017). Instead of single point analyses, orientation maps consisting of hundreds of EBSD point determinations were conducted for each grain. Using the *HKL CHANNEL5* EBSD post-processing software, orientation-maps are generated over an entire crystal, extracting hundreds to thousands of individual orientation measurements.

2. Melt inclusions

2.1 Post-entrapment crystallisation correction of melt inclusions

All melt inclusion (MI) compositions (n=28) were corrected for post-entrapment crystallization (PEC) that took place during natural quenching. Naturally quenched melt inclusions and their host minerals (olivine) were analysed by EMPA. For olivine-hosted MIs the equilibrium between olivine and silicate melt was inspected based on the partitioning of Fe and Mg between these two phases (K_D=0.335±0.01 of Shea et al. 2022). These calculations suggest that all MIs were affected by various degrees of post-entrapment crystallization and diffusion, such that their compositions should be corrected for Fe-loss. For these corrections we determined the forsterite contents of olivines in equilibrium with a range of basaltic liquid compositions (with

MgO-contents ranging between 5.4 and 8.4 wt%; Rhodes 1988; Davis et al. 2003; Couperthwaite et al. 2022) from Mauna Loa (including groundmass glasses from this study) using the same equilibrium criterion stated above (all glass data are provided in table S12). Plotting the FeO-content of these basaltic liquids as the function of Fo-contents of their equilibrium olivines helped us to determine the original FeO-content (FeO*) of the melt inclusions for each host olivine before post-entrapment modification (Fig. S1). These FeO*-contents were used as an input parameter for the corrections using the Petrolog3 software of Danyushevsky and Plechov (2011). Corrections were carried out at oxygen fugacity (fO_2) conditions of FMQ = 0, using the mineral melt model of Roeder and Emslie (1970) and the fO_2 model of Kress and Carmichael (1988). The corrected MI compositions were plotted again with previously analysed basaltic liquid compositions to verify that MI compositions followed the chemical trends typical of Mauna Loa liquid compositions. The correction procedure provided a good match with Mauna Loa liquid compositions for the majority of melt inclusions hosted in olivines with forsterite contents Fo_{82-89}.

3. Diffusion modelling

Combined diffusion and growth (CDG) modelling

The model used is essentially that of Couperthwaite et al (2021). It is a one-dimensional model that starts with an initially homogenous crystal core set at the core plateau value. The exterior of the crystal core is in contact with melt at a specific temperature, and it is the temperature which determines the equilibrium forsterite value to which the crystal edge will equilibrate. In addition, a crystal growth rate operates such that a new growth increment is added at the current equilibrium value when accumulated growth would equal a new "pixel" at the melt interface. Time is iterated incrementally and diffusion (and any necessary growth) applied at each time step; the exterior melt is also allowed to cool, causing the exterior forsterite equilibrium to migrate along a liquidus. This means that the boundary condition at the grain edge is controlled

by the T-X_{Fo} relation of the external melt, which can be determined using software such as *Petrolog3* (Danyushevsky and Plechov, 2011).

In the original implementation, Couperthwaite et al (2021) used this model type to considerably improve the quality of fit to measured normal zonation profiles than *Autodiff* alone could manage, using variable external boundary conditions coupled to crystal growth. Simply by inputting a higher initial temperature than the core equilibrium, it is possible to start modelling a reverse zone which will, during cooling, migrate into a normal zoned profile at the crystal edge as the temperature descends below that of the core equilibrium. This allows simultaneous modelling of the reverse and normal aspects of a profile, the ultimate shape of which is controlled by three main parameters: the initial peak temperature, the cooling rate, and the crystal growth rate. The instantaneous exterior boundary condition is a function of temperature, and the fO_2 is also dictated by temperature, by reference to a redox buffer (in this case QFM, from Kress and Carmichael 1988). Diffusivity is controlled directly by the temperature, but all the parameters that feed into it are either functions of temperature (external boundary condition, redox condition) or are fixed (diffusion anisotropy and frame of reference within the crystal).

In order to conduct these models, a parameterisation of the equilibrium forsterite composition as a function of magma temperature is necessary. This was calculated using the PEC-corrected composition of the most primitive melt inclusions from sample ML58D as the input melt, and modelling this melt composition using the software *Petrolog3* (Danyushevsky and Plechov 2011) with the crystallisation parameters of Ariskin et al. (1993) for olivine, plagioclase and clinopyroxene to determine the T-X_{Fo} relationship. The resulting curve was parameterised in several stages and incorporated into the model, with the T-X_{Fo} path broken into stages to account for kinks that arise due to the saturation of new mineral phases.

The models presented in figure 7 for type 4 and type 5 olivine were all modelled using this combined approach, with manual iteration and solution of the three parameters of maximum

temperature, growth rate, and cooling rate. The full dataset of 12 crystals modelled with a combined diffusion and growth (CDG) model is given in table S10. Growth rates range from zero to a maximum of 2.7×10^{-10} ms^{-1}, with most crystals between 2×10^{-11} ms^{-1} and 6×10^{-11} ms^{-1}. Peak temperatures show a cluster of crystals suggesting peak temperatures of ~1285°C and another cluster around 1210°C. Cooling rates are variable, but lie in the range between 0.018 and 0.4 degrees per hour. Altogether these 12 crystals yield combined diffusion and growth times between 4 days and 120 days, comparable to the *Autodiff* models for the more simply-zoned crystals. Expressing an uncertainty on these results is not entirely simple (and would require iteration through the full input parameter space) but we would anticipate it to be at least equal in magnitude to the *Autodiff* data. Work continues on developing the software in a similar manner to that of Mutch et al. (2021). The modelling of the complex profiles using a non-isothermal combined diffusion and growth model shows that more complex modelling is able to reconcile the reverse zones with the immediately adjacent normal-zoned crystal rims in a single cycle of heating and then cooling with growth. It has always been true to say that more complex diffusion models will probably better approach natural reality but it is only recently that this is becoming more commonplace across the many input parameters of initial zoning, temperature history and boundary conditions (e.g., Petrone et al. 2016; Couperthwaite et al. 2021; Mutch et al. 2021; this study).

4. Supplementary figures

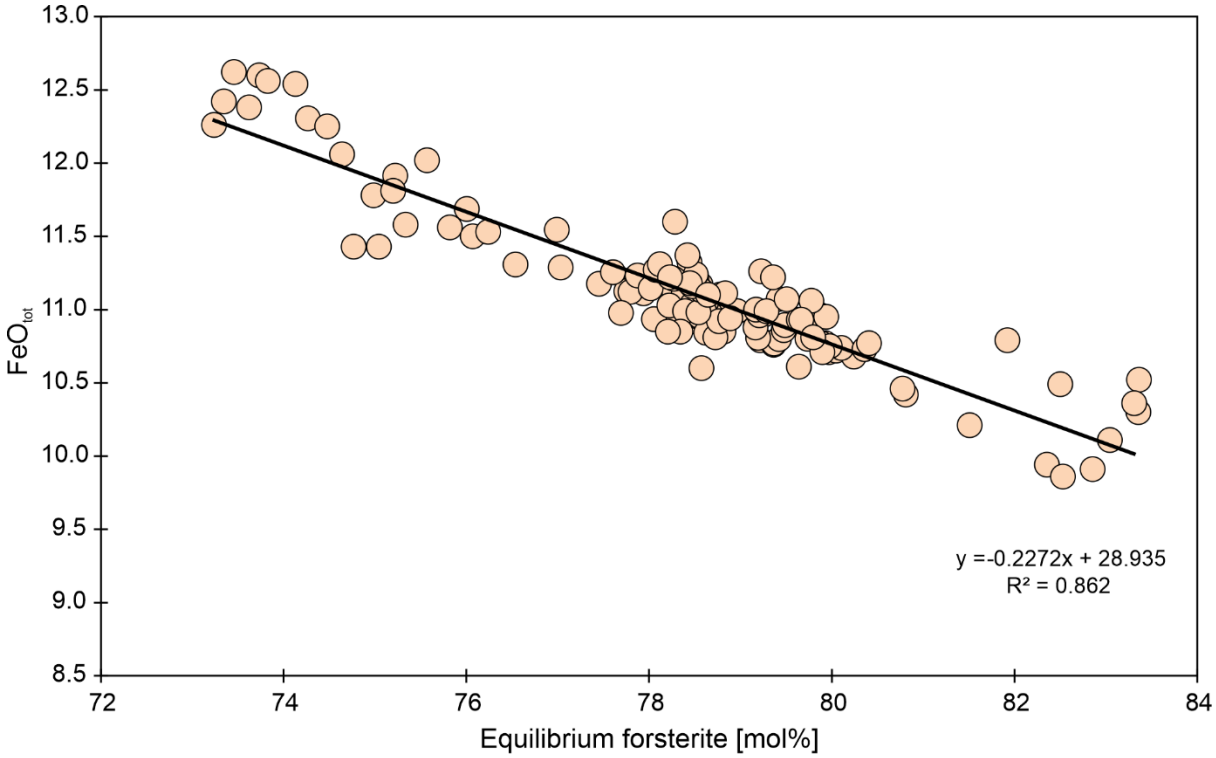

Supplementary Figure S1. Regression curve for correcting PEC in olivine-hosted melt inclusions. Equilibrium forsterite content versus FeO_{tot} of Mauna Loa glasses (groundmass glasses: Rhodes 1988; Davis et al. 2003; Couperthwaite et al. 2022 and this study; table S12). Equilibrium forsterite content was calculated using the updated K_D value of 0.335±0.01 of Shea et al. (2022) for tholeiites. The regression equation was used to estimate the original FeO* of the olivine-hosted melt inclusions at any given forsterite content following the procedure outlined in Kahl et al. (2021) and Caracciolo et al. (2020).

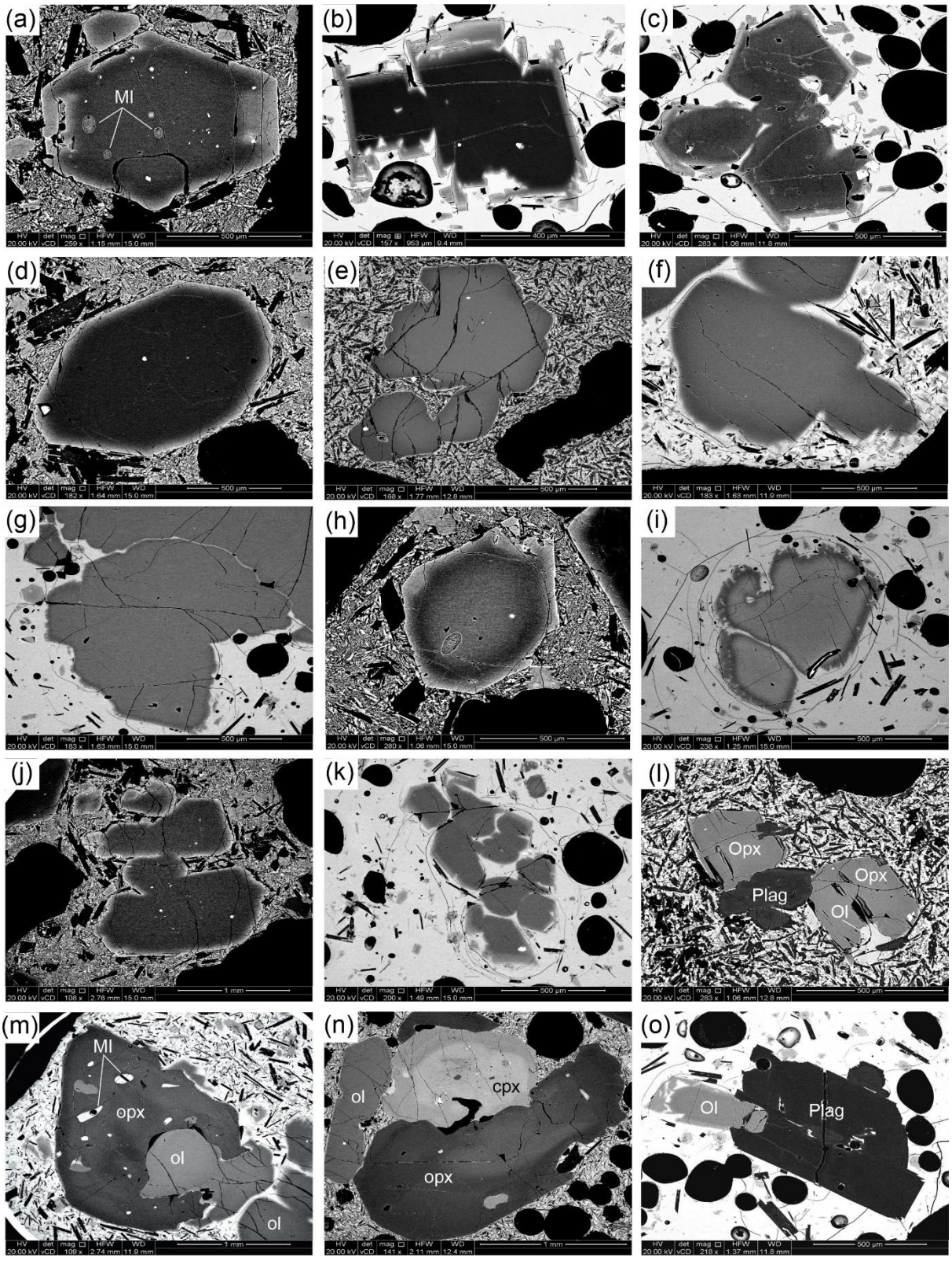

Supplementary Figure S2. (a-l) Backscatter electron (BSE) images documenting olivine zoning and textural features. (a-c) Normal and complexly zoned olivine macrocrysts with sub- to anhedral rims with dendritic morphologies indicative of fast growth or fast undercooling. (d-f) Large sub- to anhedral olivine macrocrysts with normal zoning and sub-rounded crystal faces. (g-i) Reversely zoned olivine macrocrysts with low-forsterite cores overgrown by forsterite-rich rims. (j-o) Glomerophyric textures. (j-k) Cluster of normally zoned, polyhedral olivines with sub- to anhedral sub-rounded rims. (l) Polymineralic clot orthopyroxene, plagioclase and olivine. (m) Poikilitic large orthopyroxene

macrocryst (Mg-rich) including melt inclusions and olivine. Note intergrowth with large anhedral olivine. Anhedral and sub-rounded crystal faces. (n) Polymineralic, gabbronoritic clot of complexly zoned orthopyroxene, reversely zoned clinopyroxene and olivine. (o) Troctolitic glomerocryst of normally zoned olivine and plagioclase. Dendritic olivine rims. Ol: Olivine; Cpx: Clinopyroxene; Opx: Orthopyroxene; Plag: Plagioclase; MI: Melt inclusion.

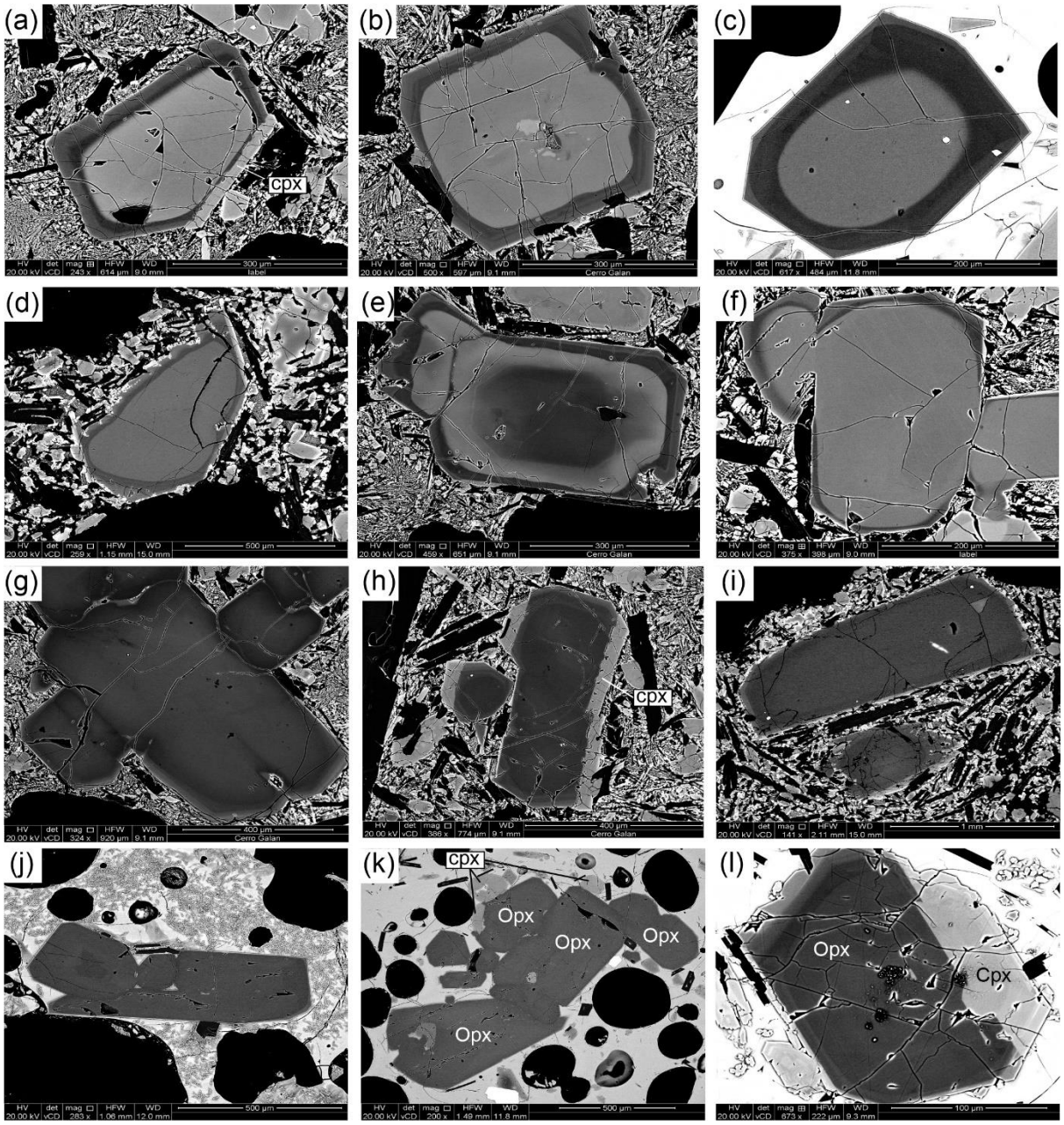

Supplementary Figure S3. (a-l) Backscatter electron (BSE) images documenting orthopyroxene zoning types and textural features. (a-f) Reverse and (e) complexly zoned orthopyroxenes containing anhedral and corroded low Mg-number cores overgrown by Mg-rich, oscillatory and sector zoned mantles, followed by euhedral to subhedral, low Mg-number rims. (e) Complexly zoned orthopyroxene with an anhedral and resorbed high-Mg-number core, followed by a low-Mg-number mantle zone and increasing Mg contents towards the rim. (g-i) Normally zoned orthopyroxene macrocrysts with Mg-rich cores and decreasing contents towards the outermost rims. (g) Monomineralic cluster of large, Mg-rich orthopyroxene crystals. (h) Crystallographically oriented overgrowth of clinopyroxene on Mg-rich orthopyroxene core. (j) Monomineralic cluster of Mg-rich orthopyroxene. (k) Glomerophyric cluster of Mg-rich orthopyroxene and clinopyroxene. (l) Crystallographically oriented intergrowth of ortho- and clinopyroxene. Note the oscillatory zoning. Opx: Orthopyroxene; Cpx: Clinopyroxene.

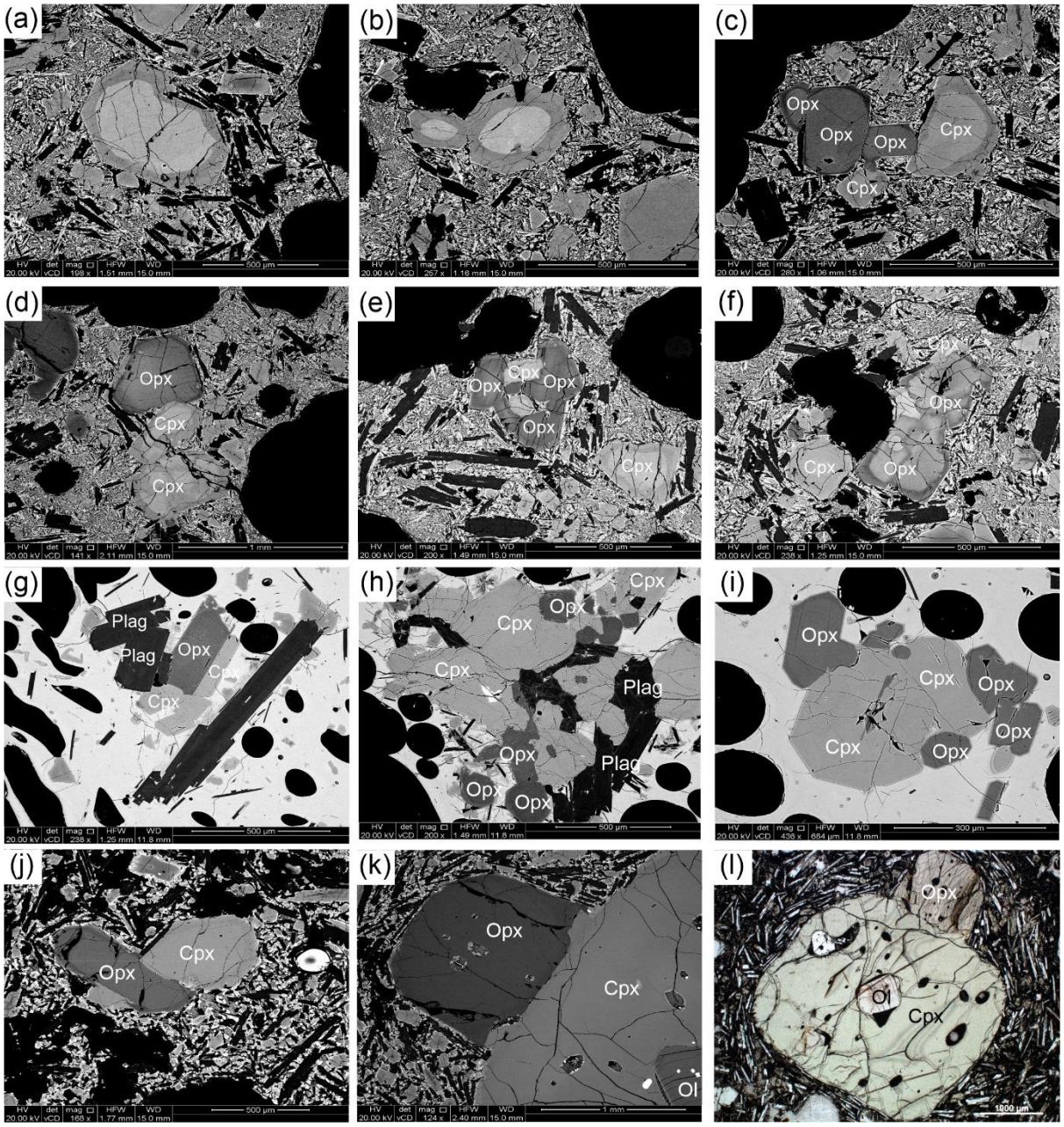

Supplementary Figure S4. (a-k) Backscatter electron (BSE) images and photomicrograph (l) documenting clinopyroxene zoning types and textural features. (a-f) Complex reversely zoned clinopyroxene crystals containing anhedral and corroded low Mg-number cores overgrown by Mg-rich, oscillatory and sector zoned mantles/ rims. Anhedral rims incorporating plagioclase microlites from the surrounding groundmass. (c-f) Glomerophyric clusters of reversely zoned clinopyroxenes and orthopyroxenes. (g-h) Gabbronoritic clots of orthopyroxene, clinopyroxene and plagioclase with interstitial glass (h). (i-k) Cluster of orthopyroxenes and clinopyroxenes. (j) Intergrowth of reversely zoned clino- and orthopyroxene. (k) Mg-rich orthopyroxene intergrown with megacrystic clinopyroxene. (l) Photomicrograph of (k) showing large, poikilitic clinopyroxene enclosing olivine. Opx: Orthopyroxene; Cpx: Clinopyroxene; Plag: Plagioclase; Ol: Olivine.

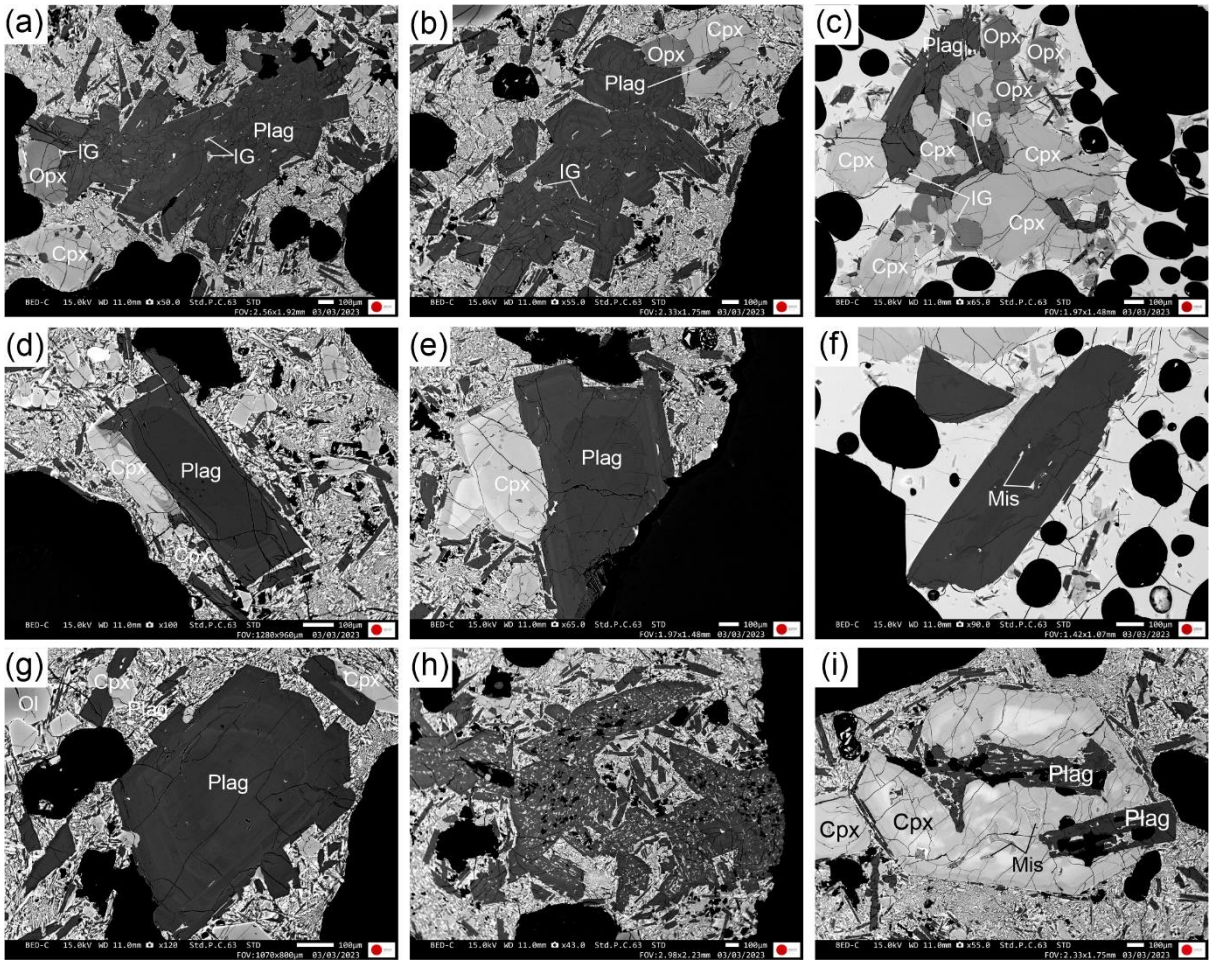

Supplementary Figure S5. (a-i) Backscatter electron (BSE) images documenting plagioclase zoning and textural features. (a-c) Gabbronoritic clusters of oscillatory zoned plagioclase, clino- and orthopyroxene. (d-e) Intergrowth of reversely zoned plagioclase and clinopyroxene. Note corroded plagioclase and clinopyroxene cores. (f-g) Rare plagioclase macrocrysts. (h) Cluster of subhedral plagioclase crystals containing strongly resorbed, spongy cores. (i) Poikilitic, euhedral clinopyroxene macrocryst enclosing strongly resorbed plagioclase crystals displaying sieve textures. Clinopyroxene displays reversely zoned outermost rims and patchy zoning in the centre. Opx: Orthopyroxene; Cpx: Clinopyroxene; Plag: Plagioclase; Ol: Olivine; IG: Interstitial glass; MIs: Melt inclusions.

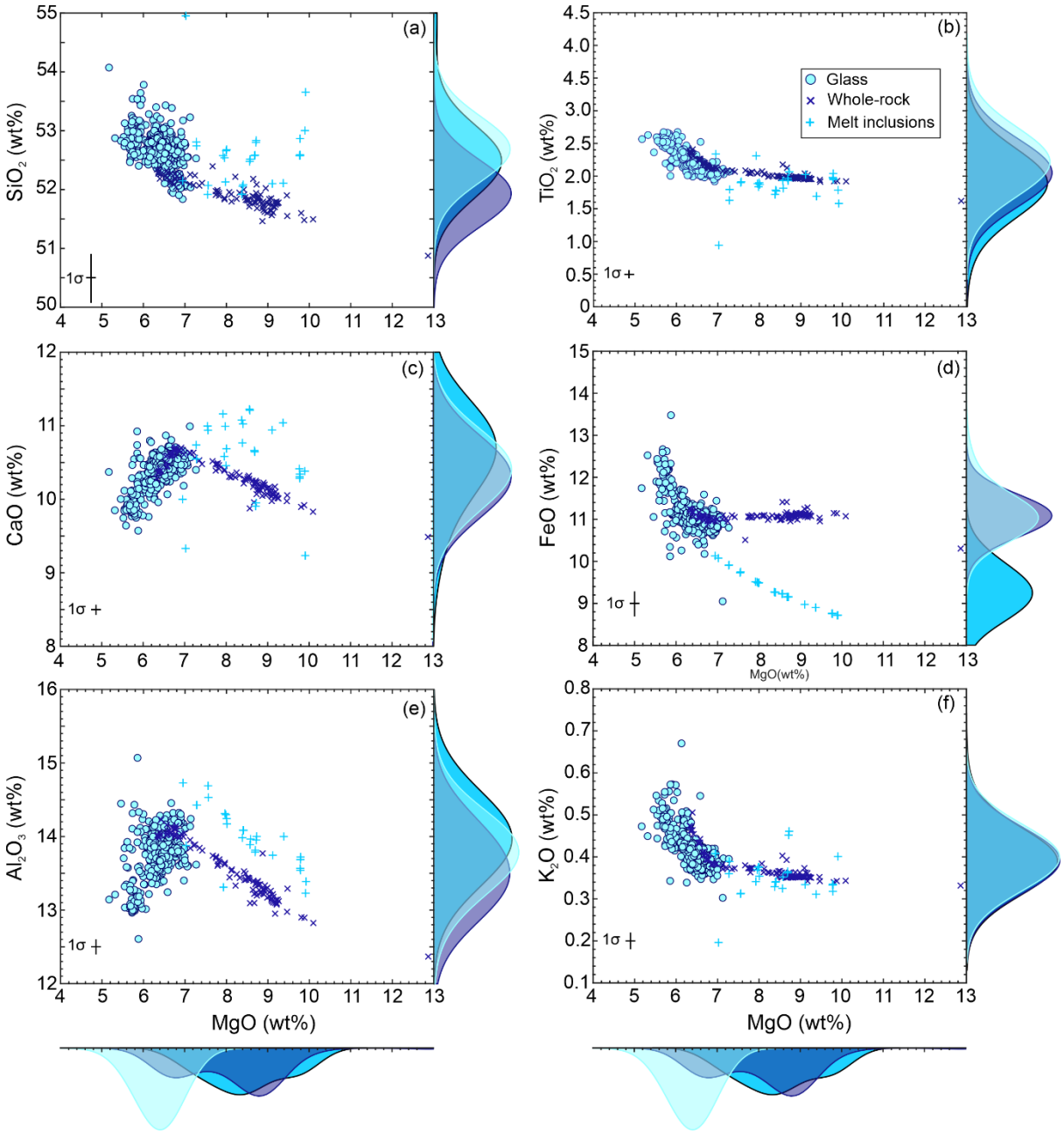

Supplementary Figure S6. (a-f) Major element versus MgO content plots of groundmass glasses, melt inclusions and whole rocks from the 1950 AD SWRZ eruption. Melt inclusions have been corrected for post-entrapment crystallization. Filled circles: Groundmass glass compositions; Dark blue crosses: Whole rock compositions; Light blue crosses: PEC-corrected melt inclusion compositions. Error bars: 1σ.

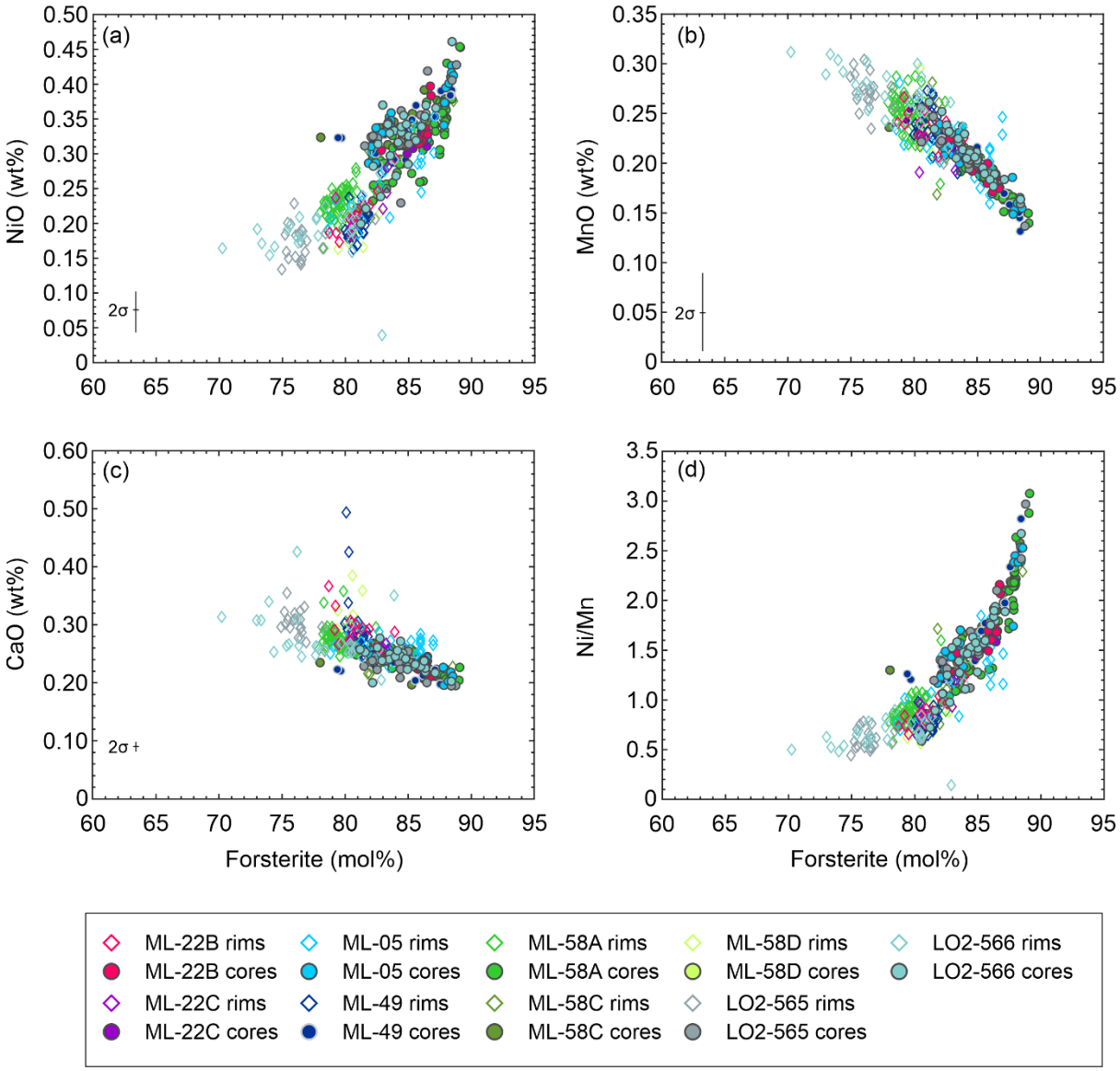

Supplementary Figure S7. Plots of minor (MnO, CaO, NiO and Ni/Mn) elements versus forsterite contents of olivine cores (filled circles) and rims (open diamonds). Forsterite =100×(Mg/[Mg+Fe]). Error bars: 2σ

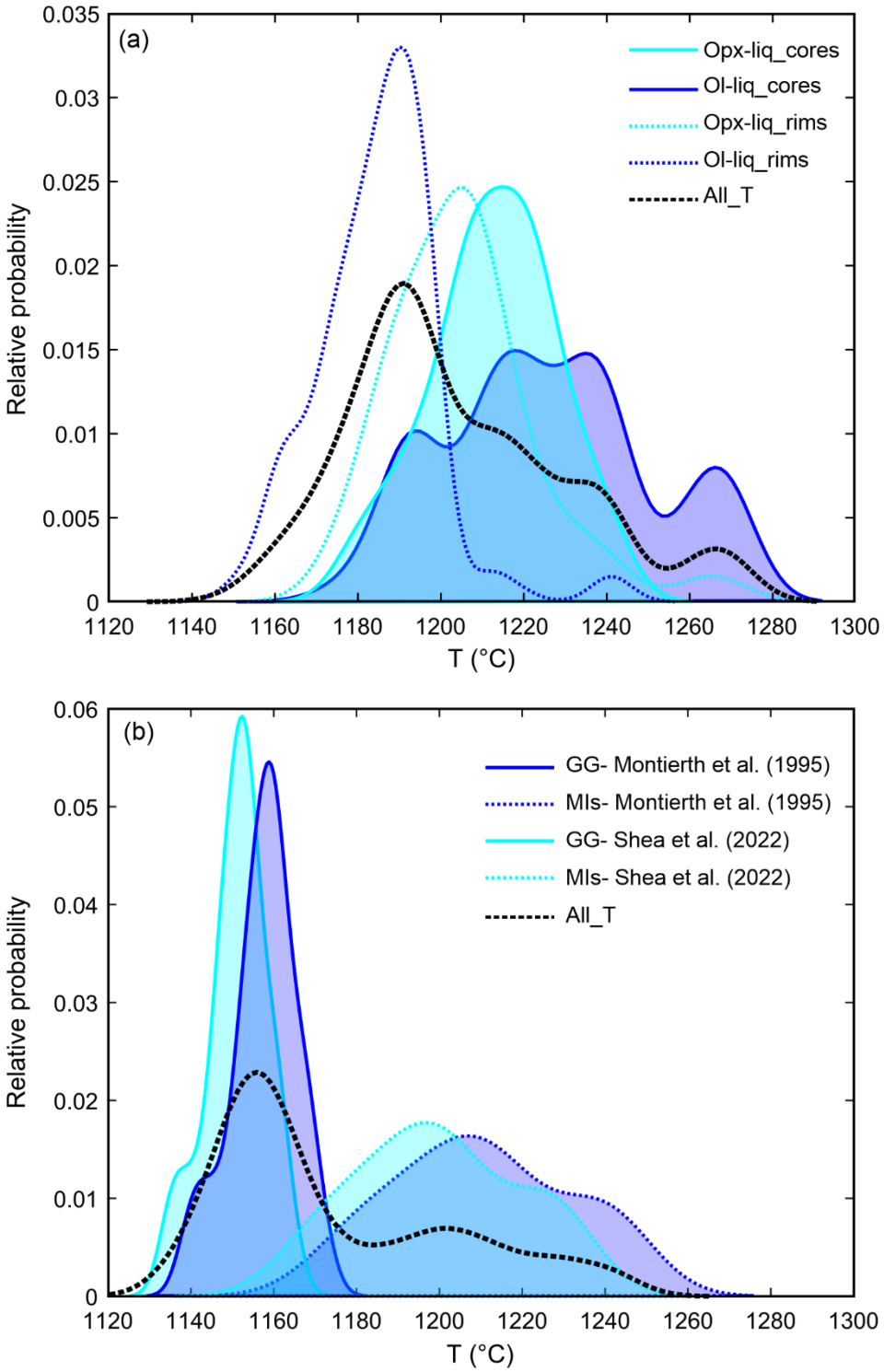

Supplementary Figure S8. Geothermometry constraints. (a) Kernel density estimates (KDEs) showing temperature distributions from mineral-melt (olivine-melt and orthopyroxene-melt; Putirka 2008) thermometry for macrocryst cores and rims. (b) KDEs showing temperature distributions from melt-only thermometry (Montierth et al. 1995; Shea et al. 2022). MIs: melt inclusions; GG: groundmass. KDEs were calculated using bandwidths of 3 to 11°C. Black stippled KDEs depict combined temperature distribution results for melt-only and mineral-melt thermometers using bandwidths of 7-9°C.

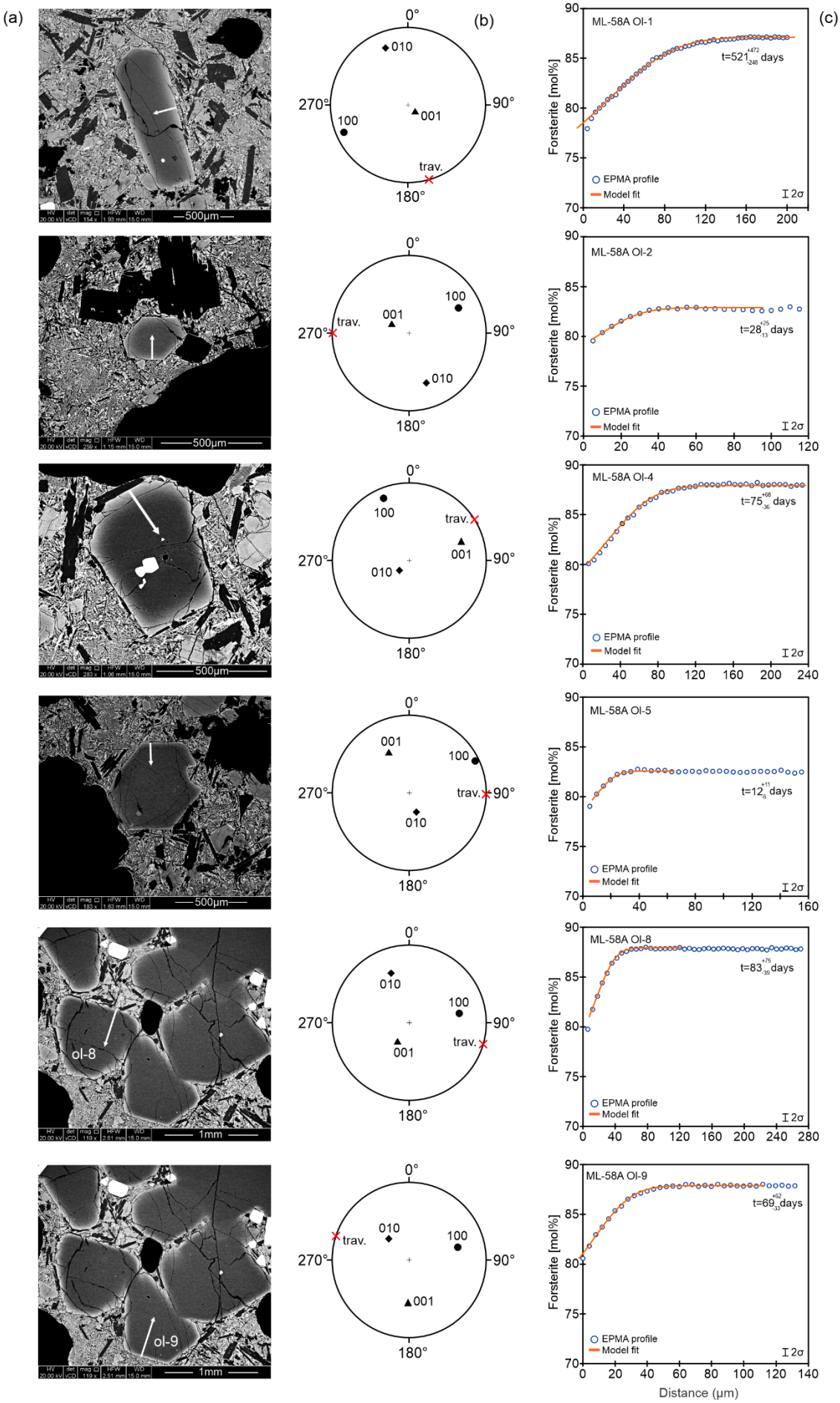

Supplementary Figure S9 - ML-58A

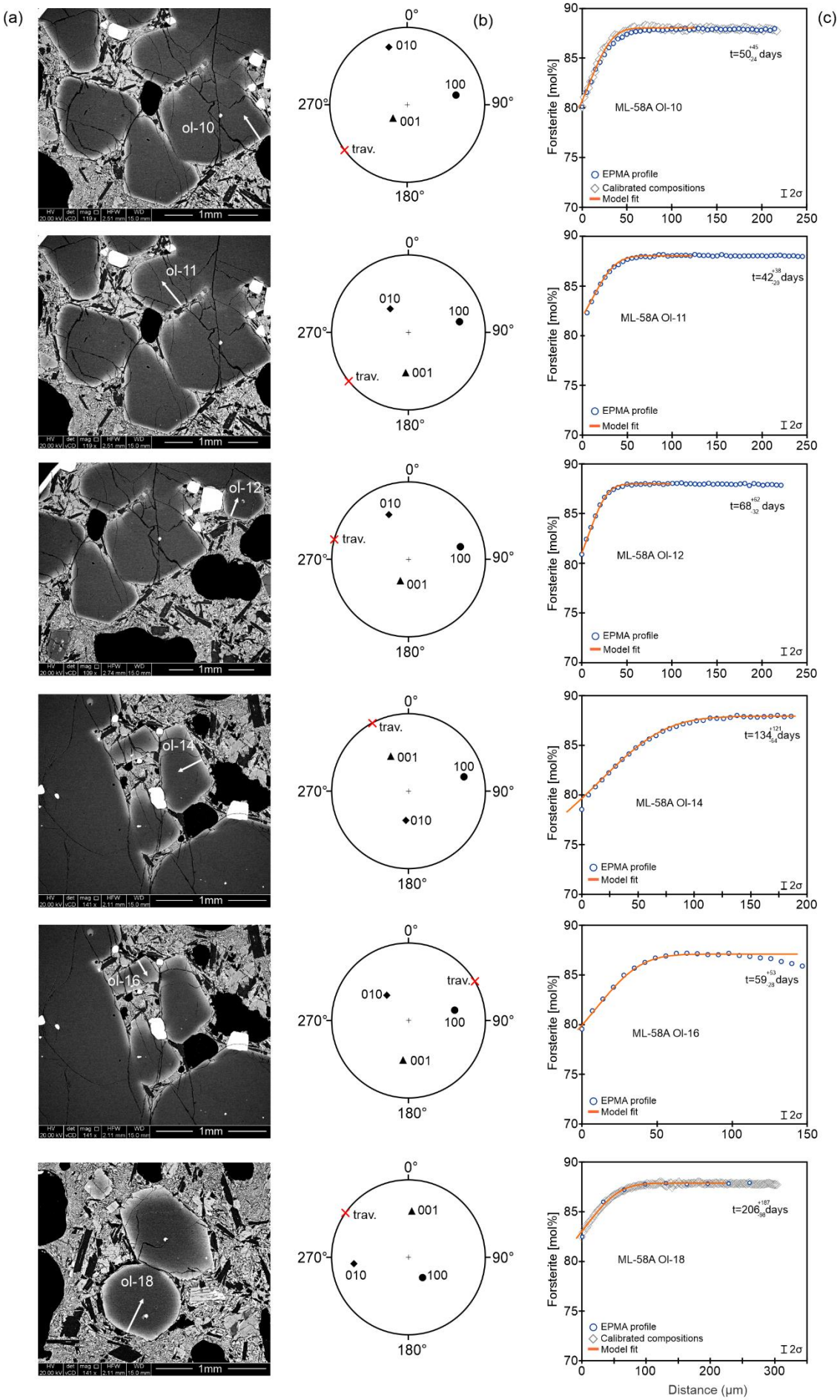

Supplementary Figure S10 - ML-58A

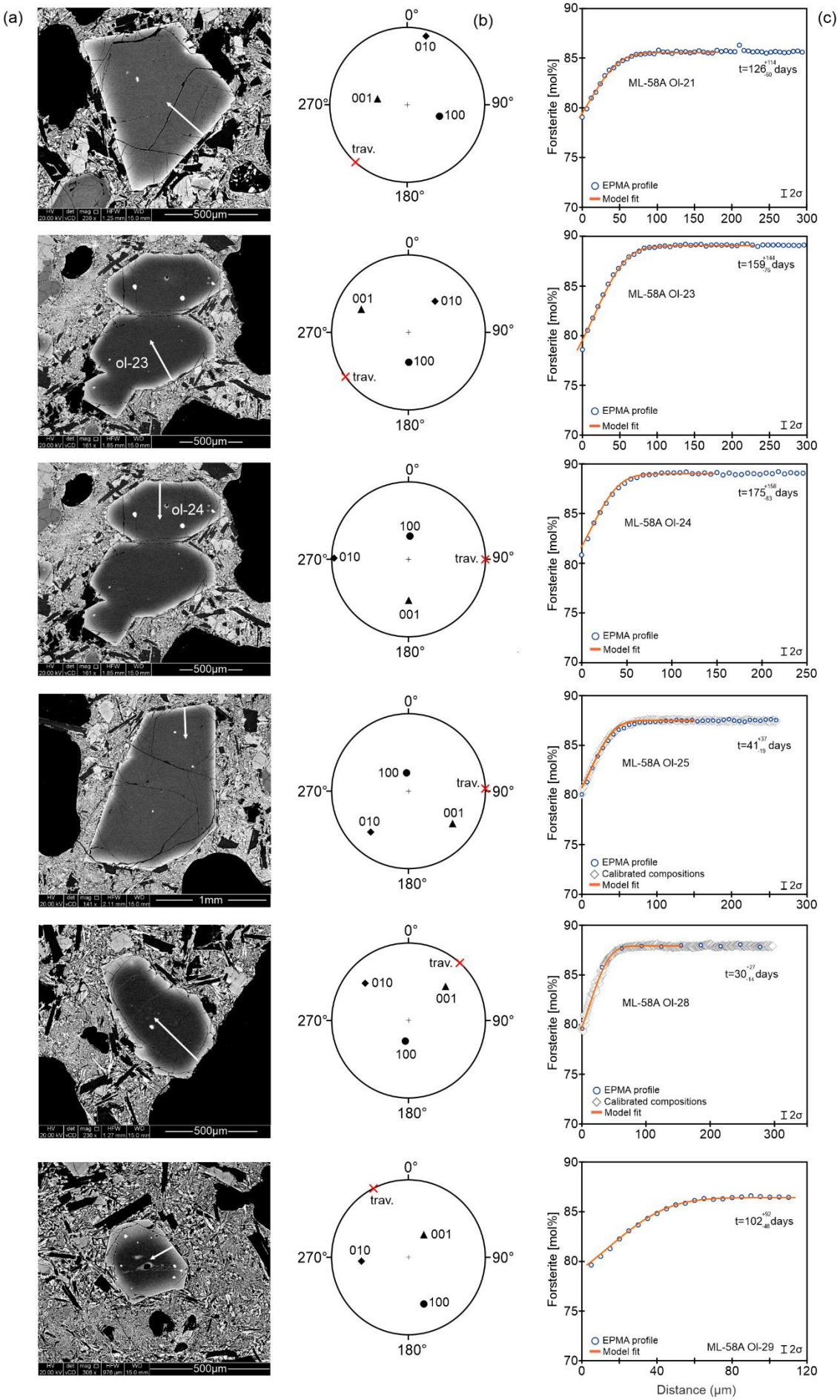

Supplementary Figure S11 - ML-58A

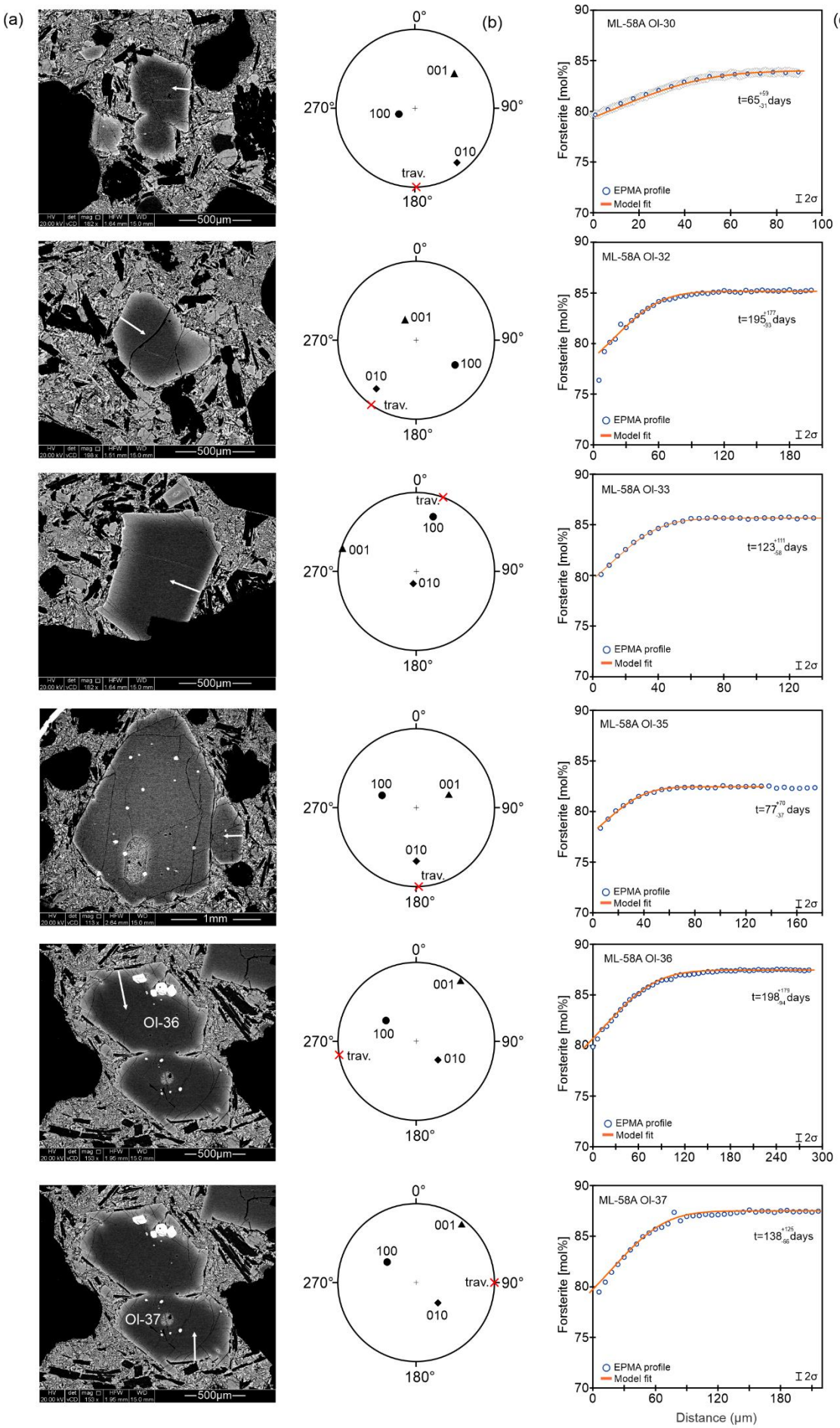

Supplementary Figure S12 - ML-58A

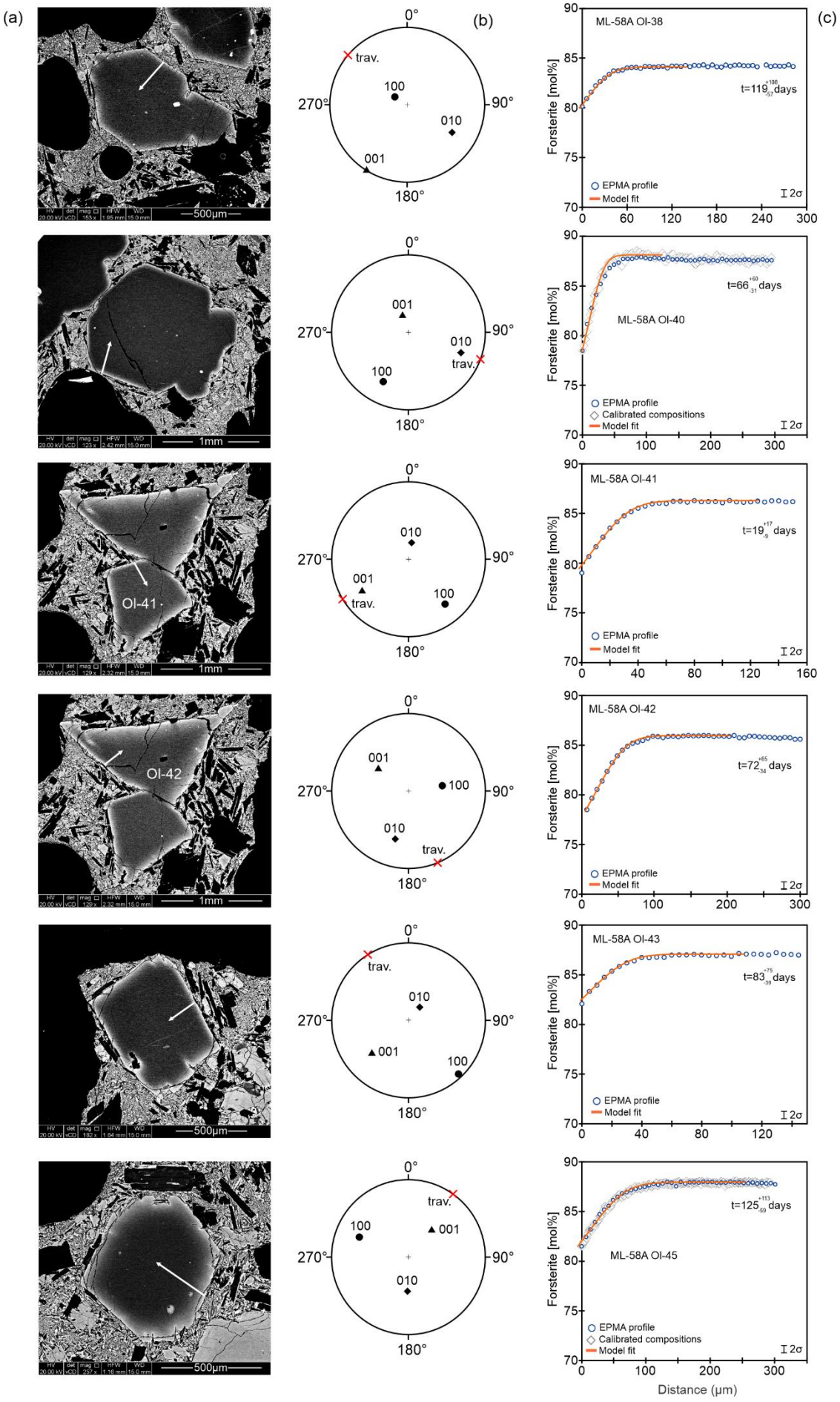

Supplementary Figure S13 - ML-58A

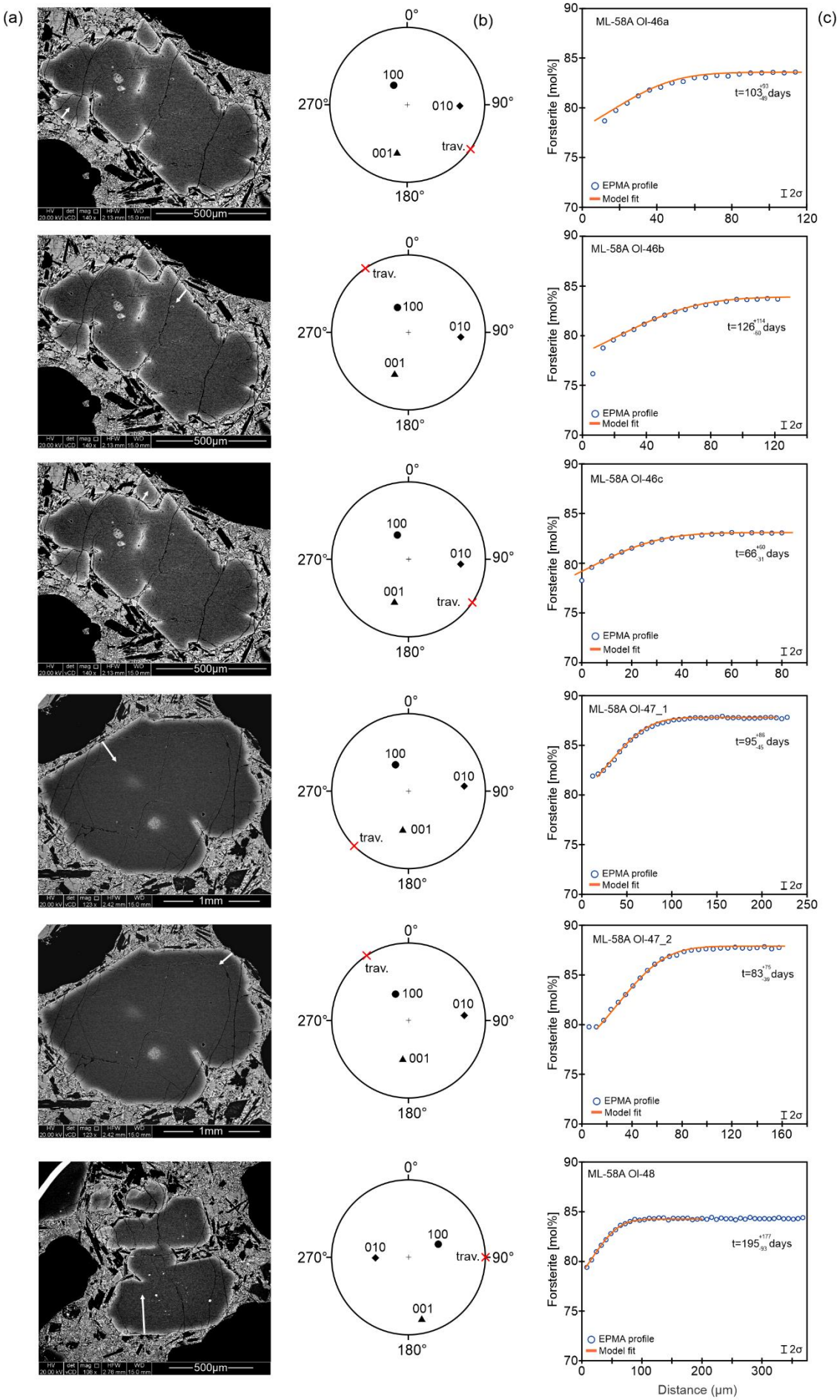

Supplementary Figure S14 - ML-58A

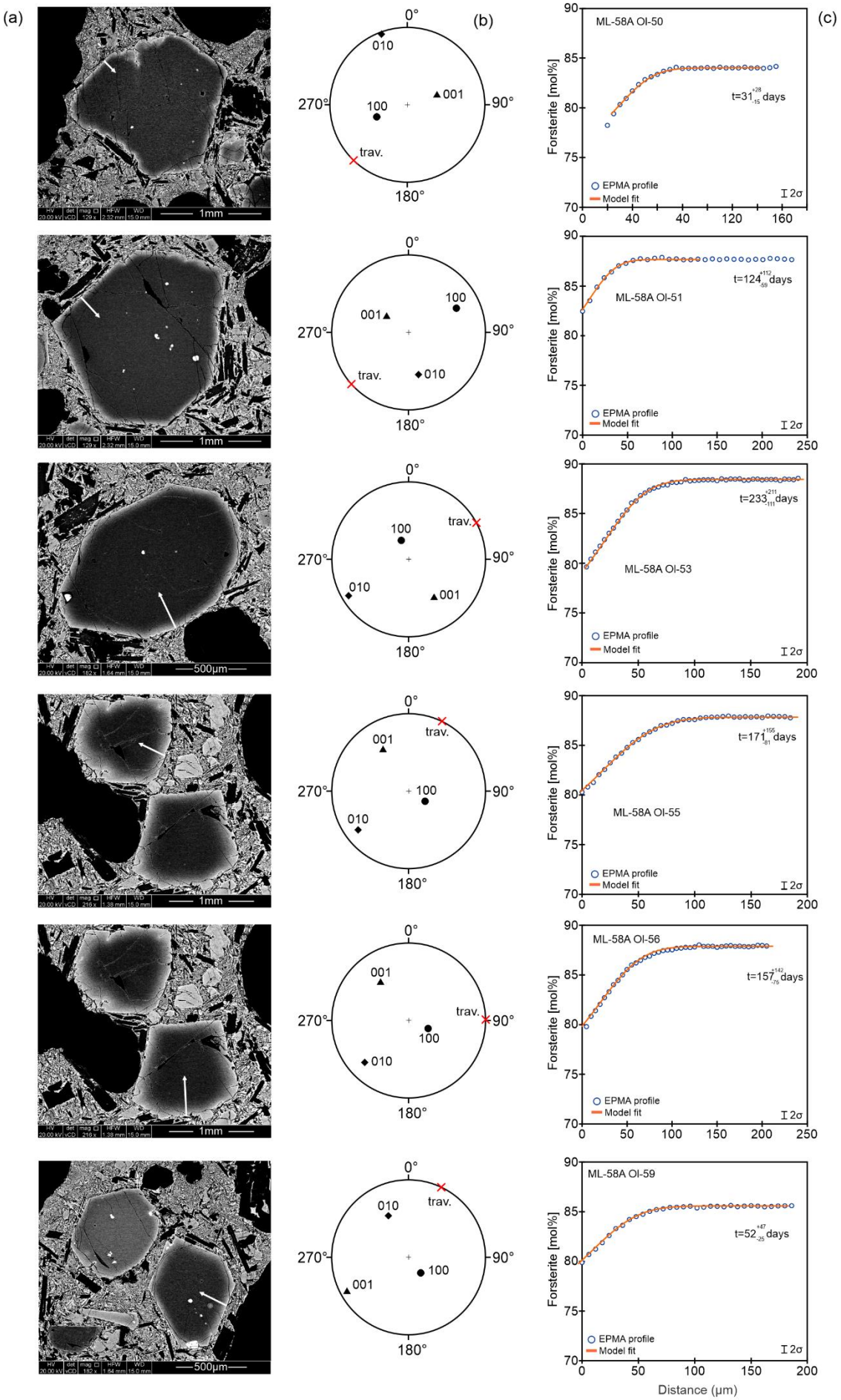

Supplementary Figure S15 - ML-58A

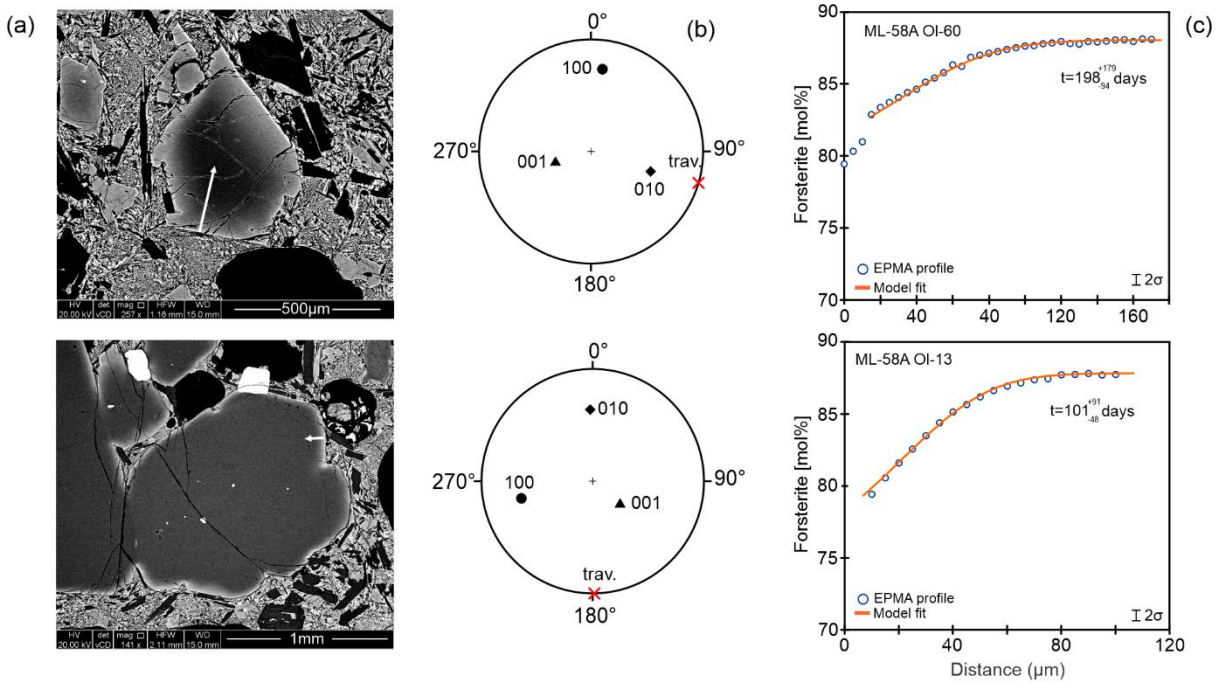

Supplementary Figure S16 - ML-58A

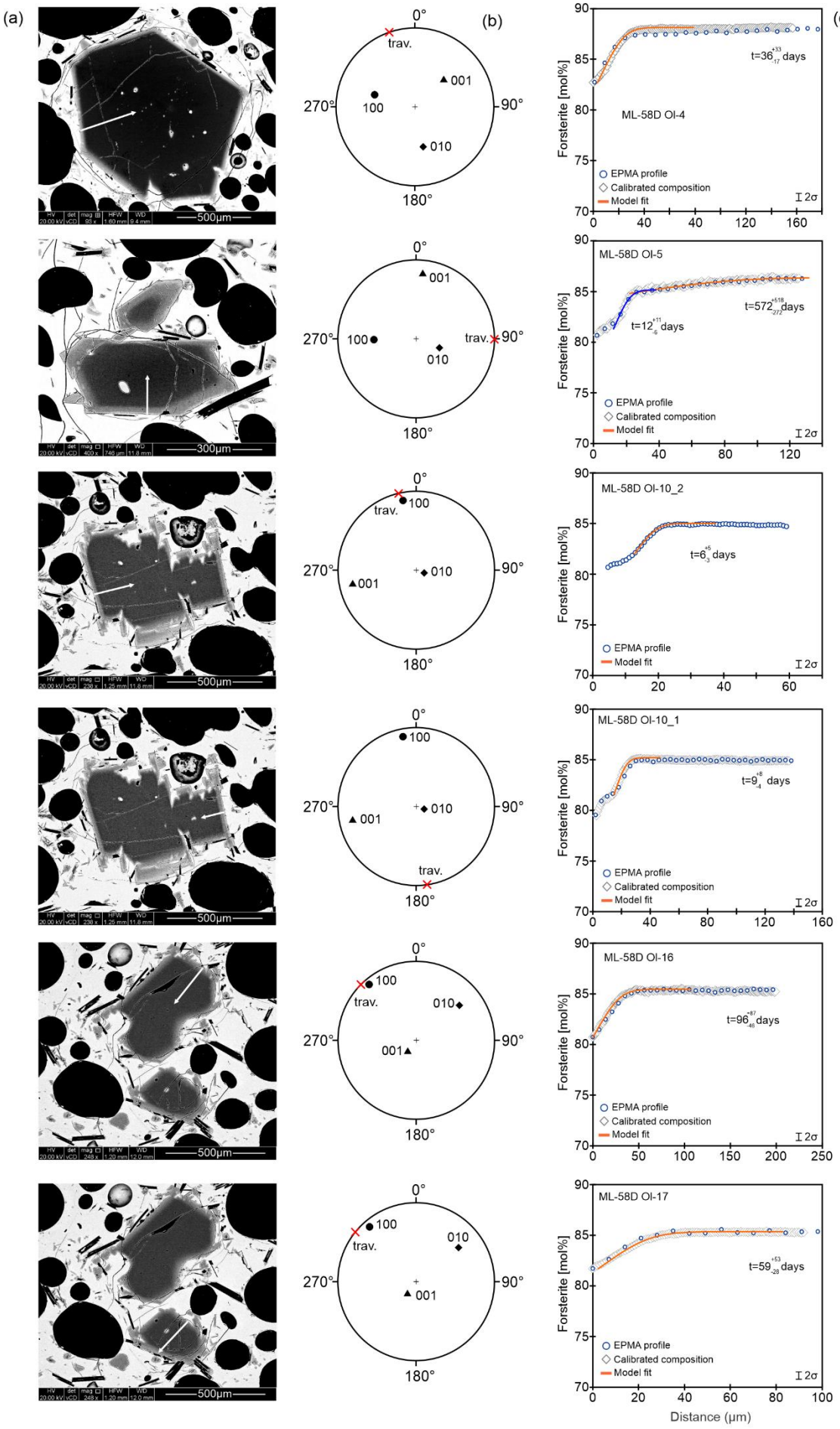

Supplementary Figure S17 - ML-58D

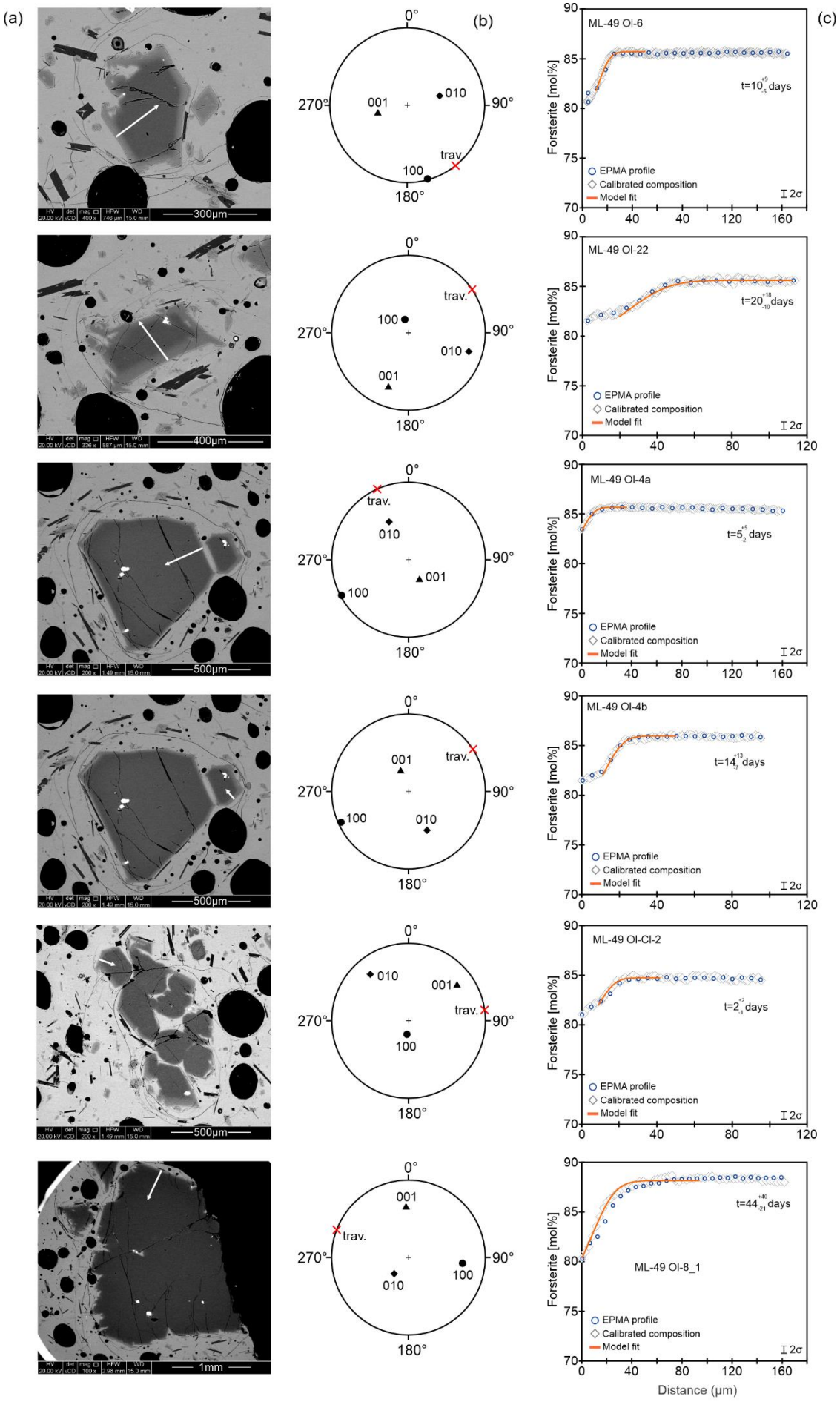

Supplementary Figure S18 - ML-49

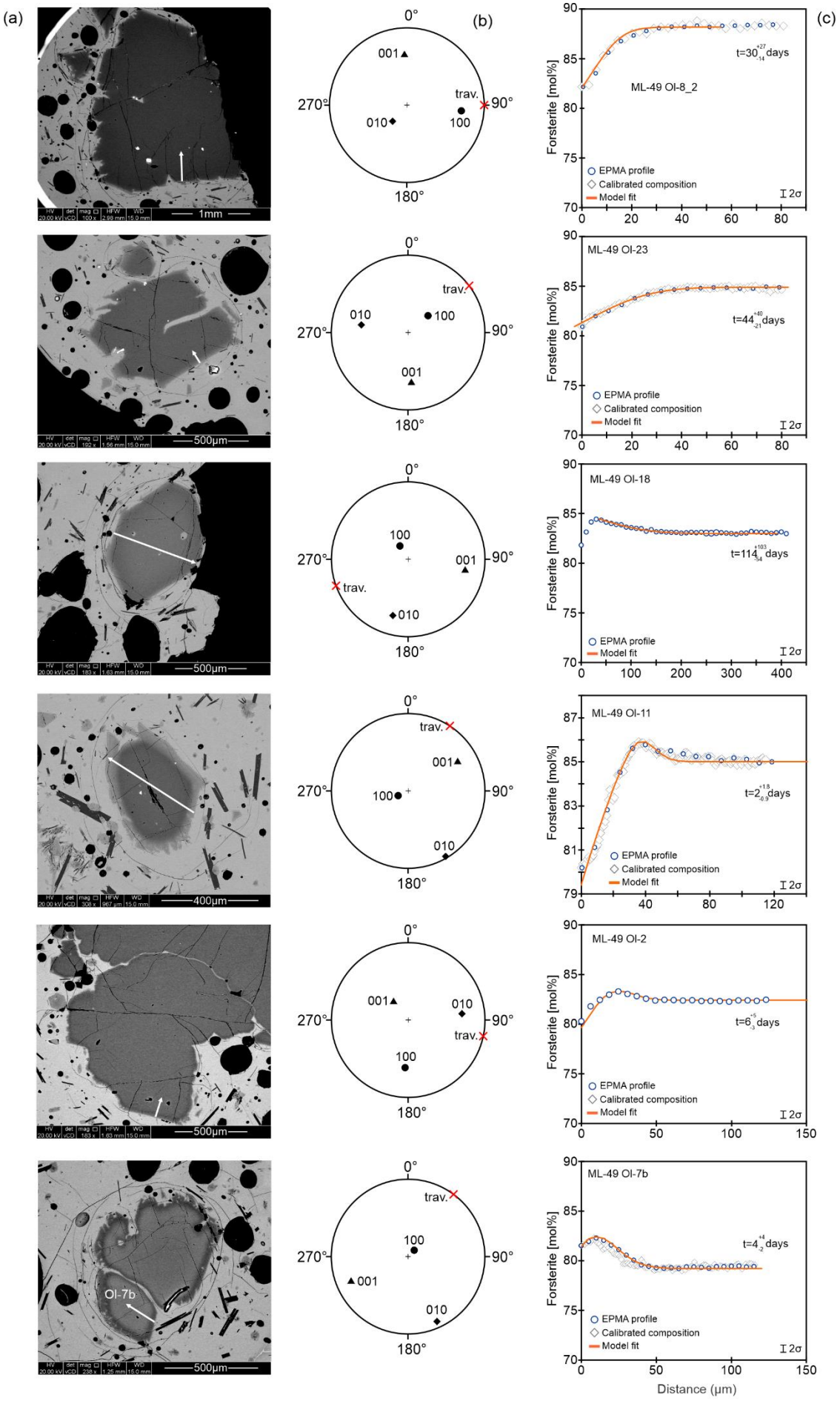

Supplementary Figure S19 - ML-49

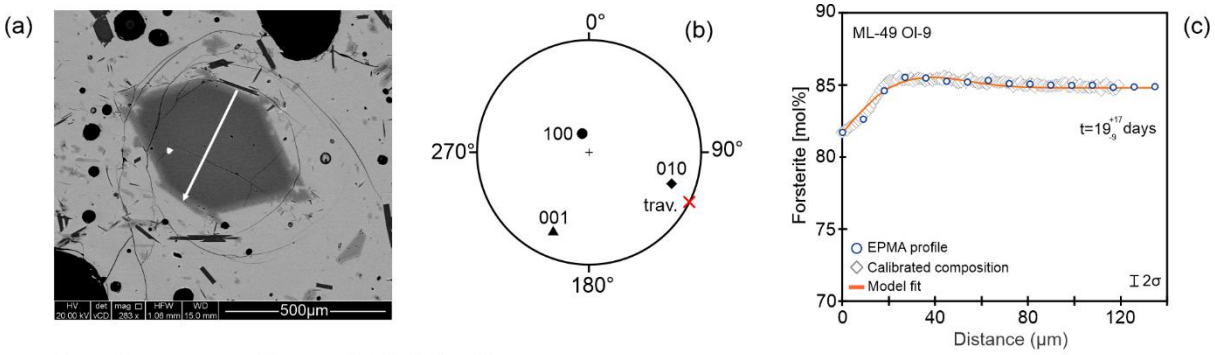

Supplementary Figure S20 -ML-49

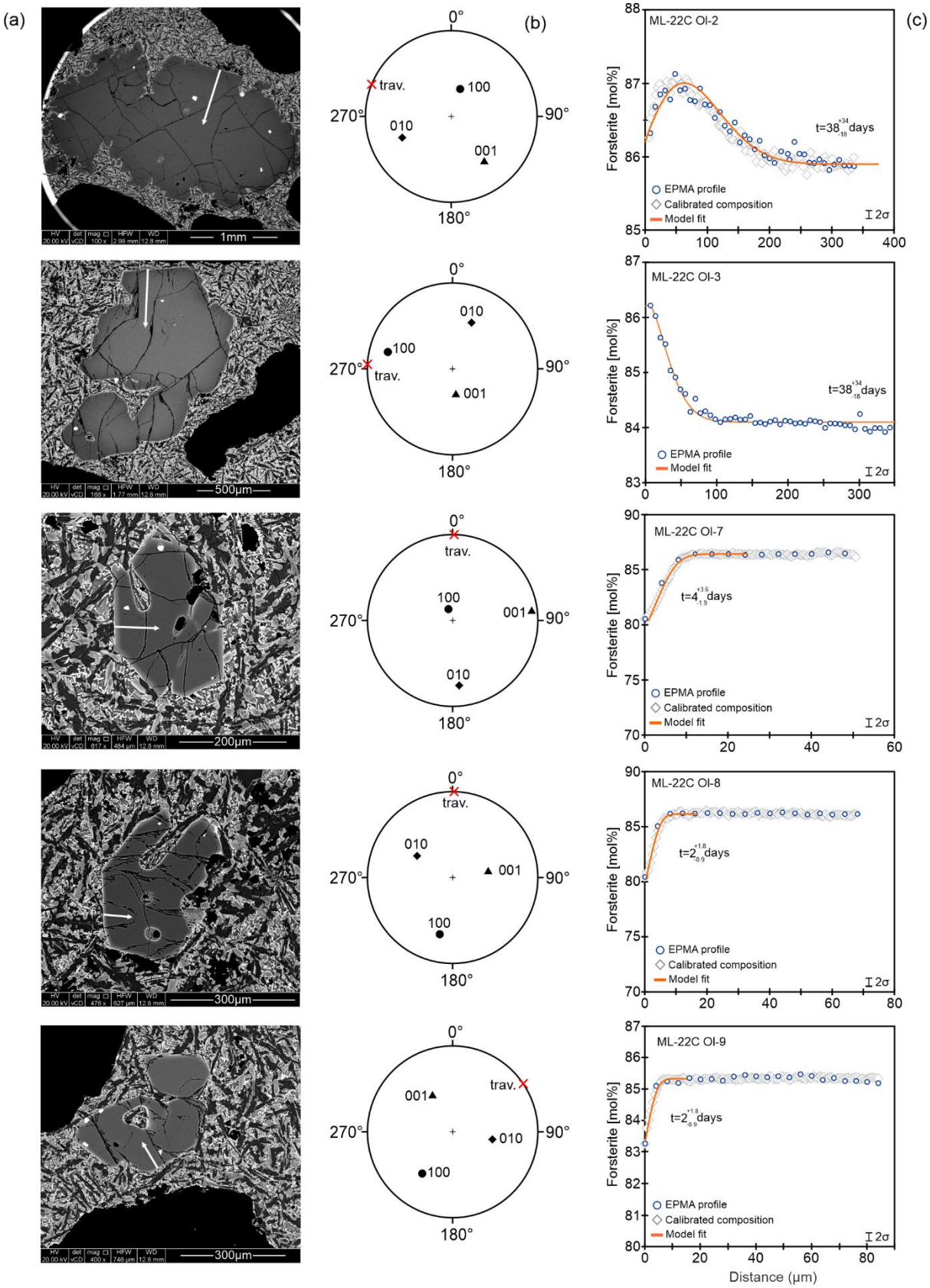

Supplementary Figure S21 - ML-22C

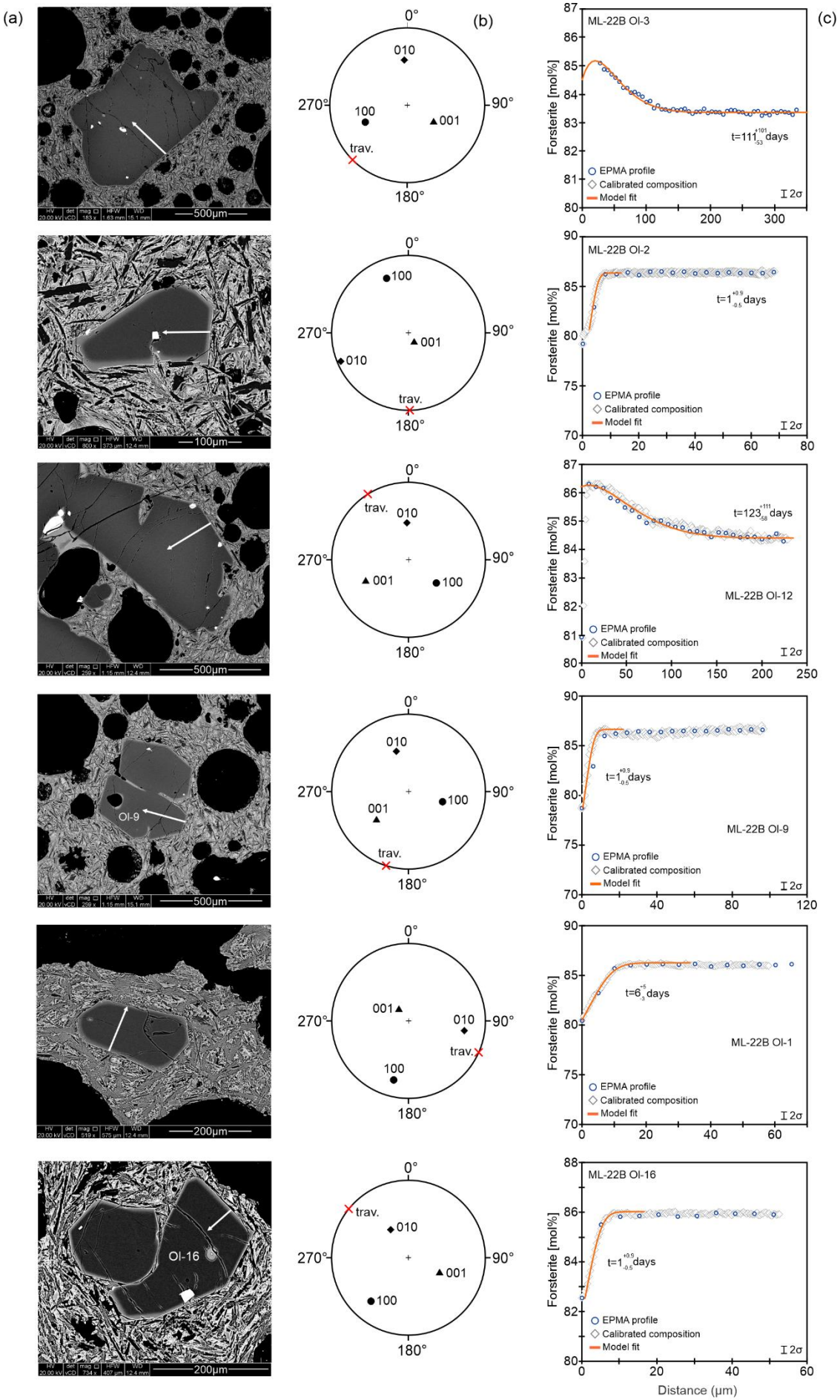

Supplementary Figure S22 - ML-22B

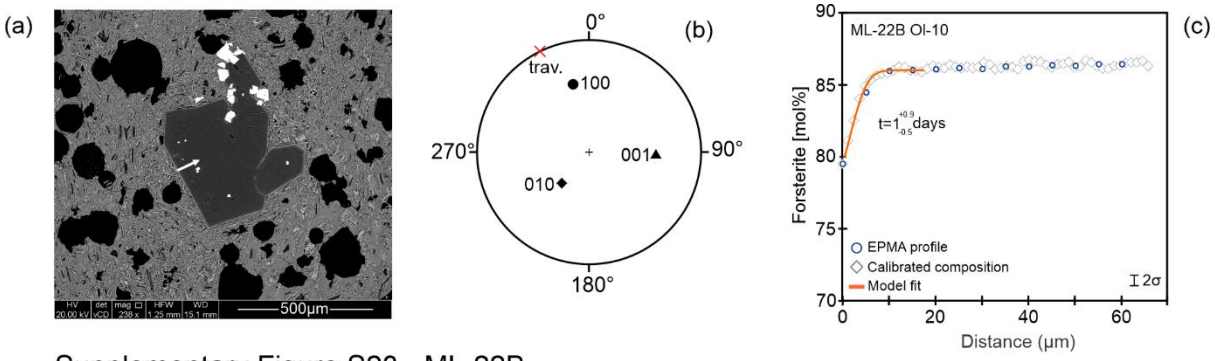

Supplementary Figure S23 - ML-22B

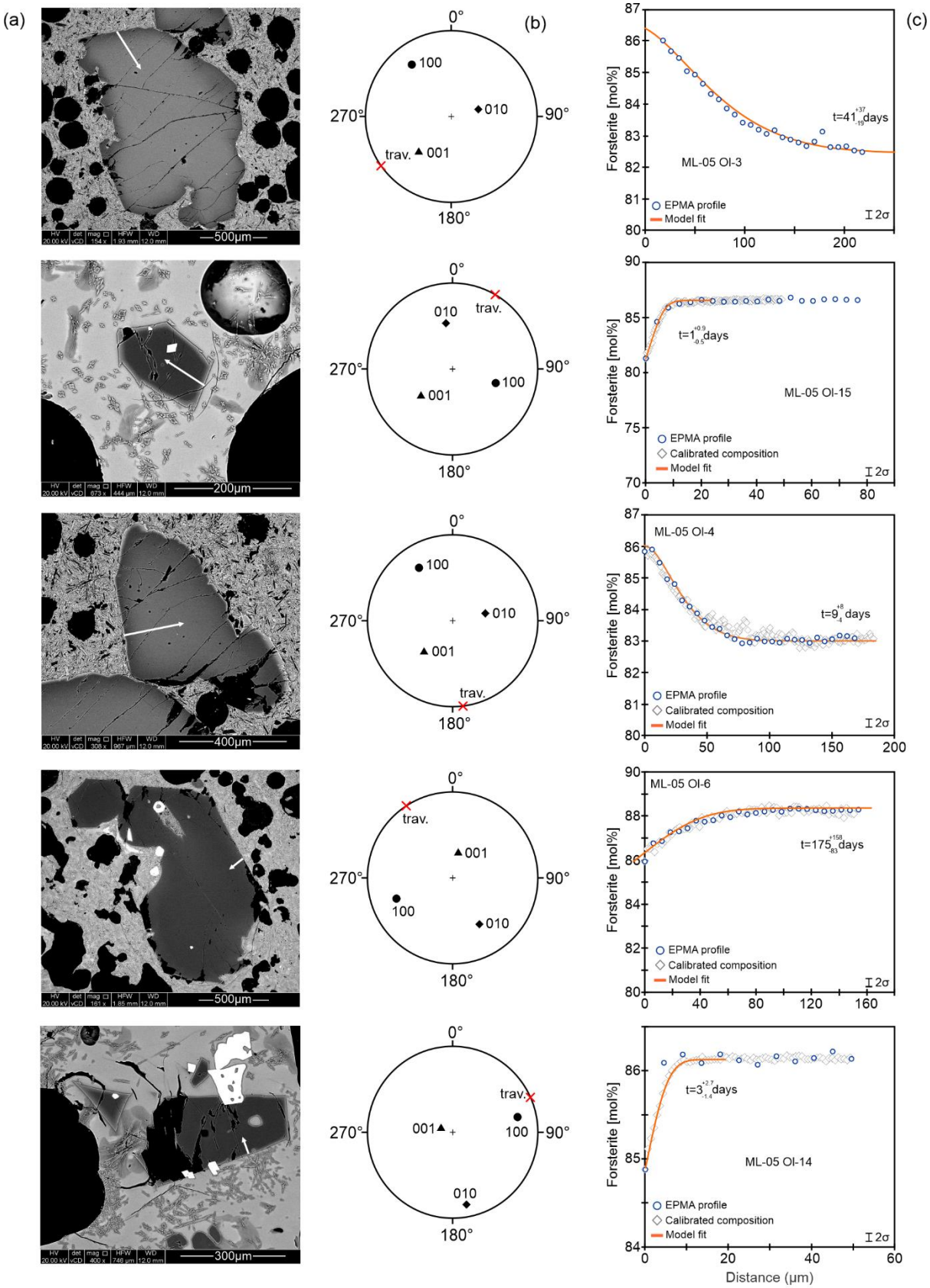

Supplementary Figure S24 - ML-05

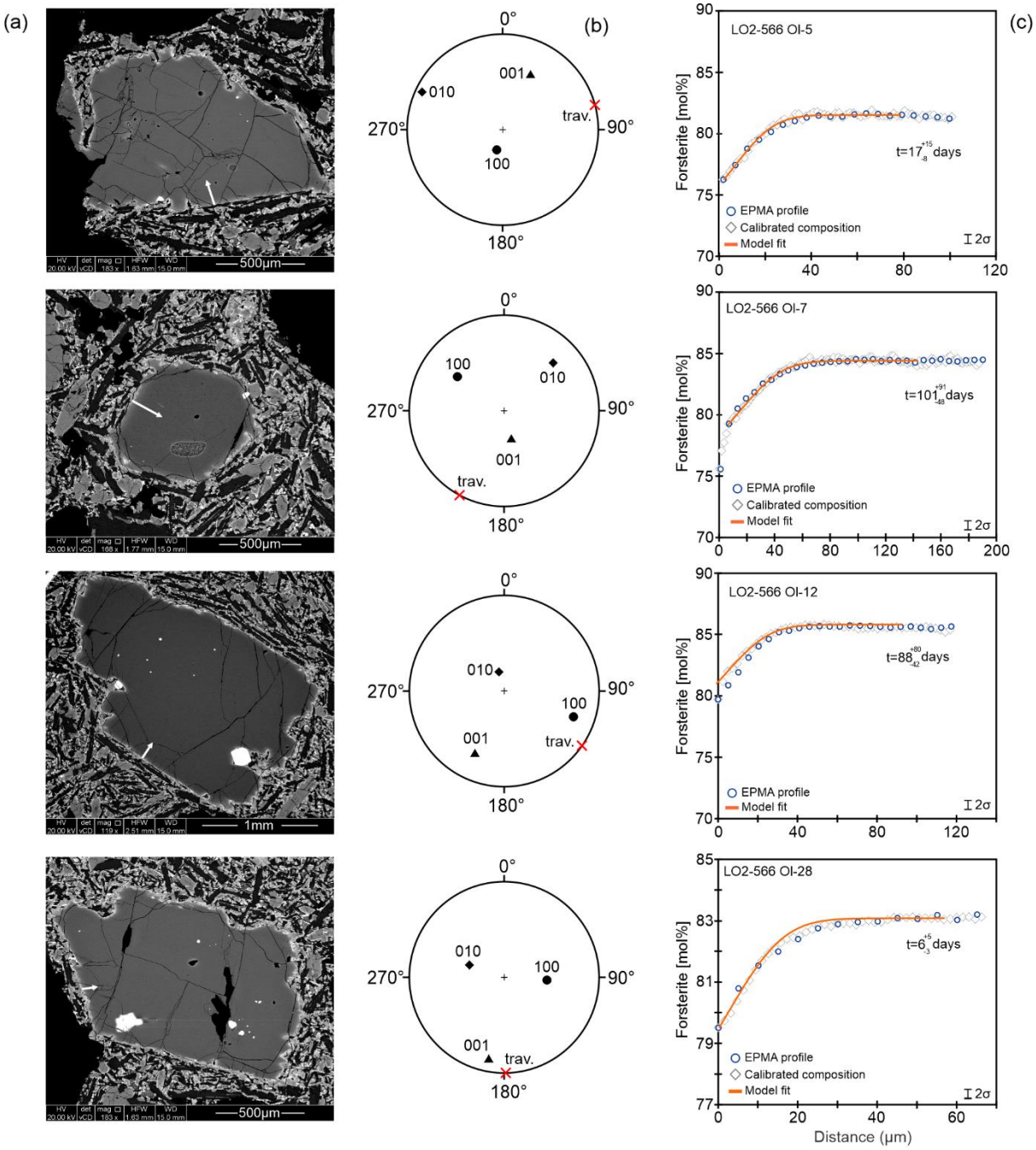

Supplementary Figure S25 - LO2-566

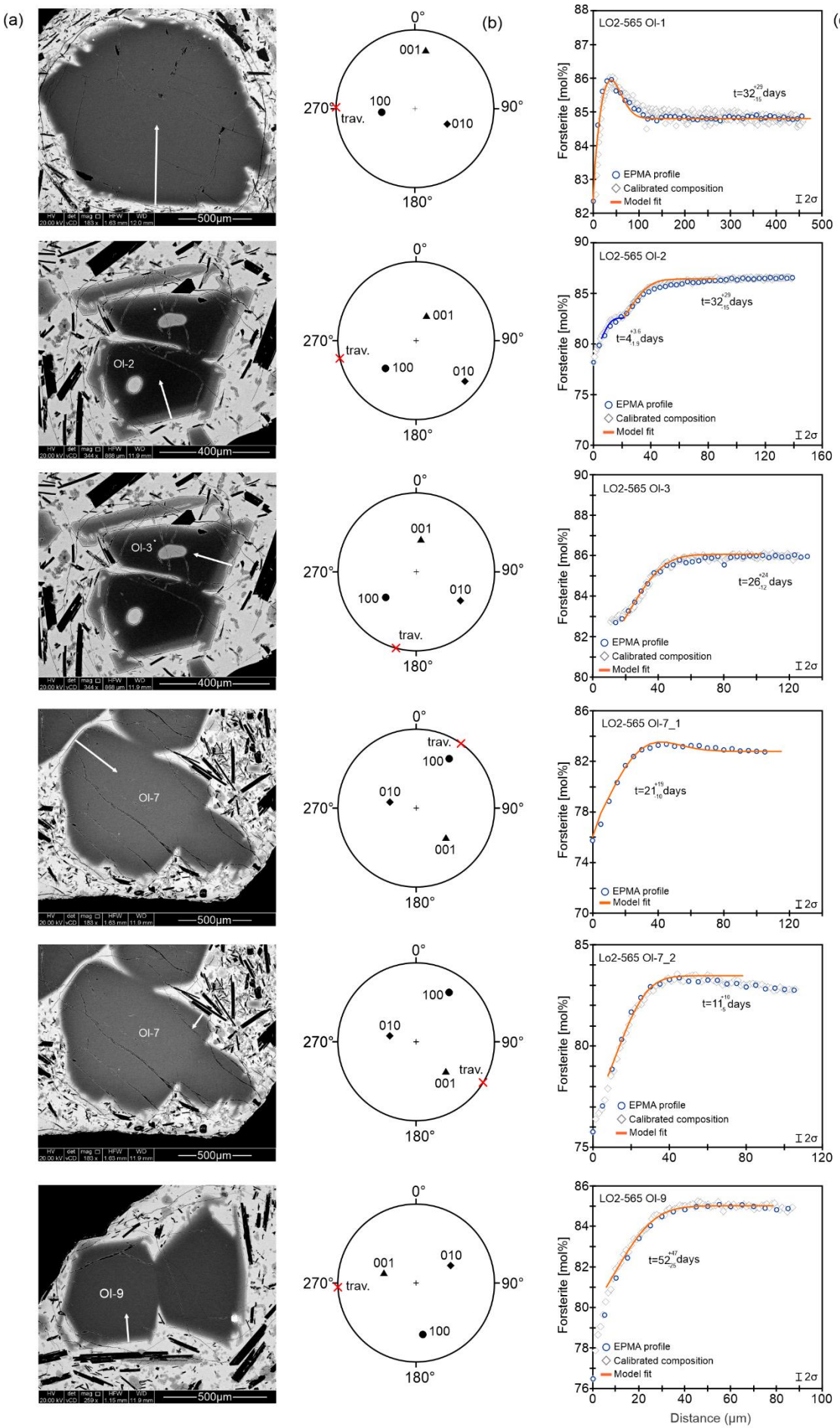

Supplementary Figure S26 - LO2-565

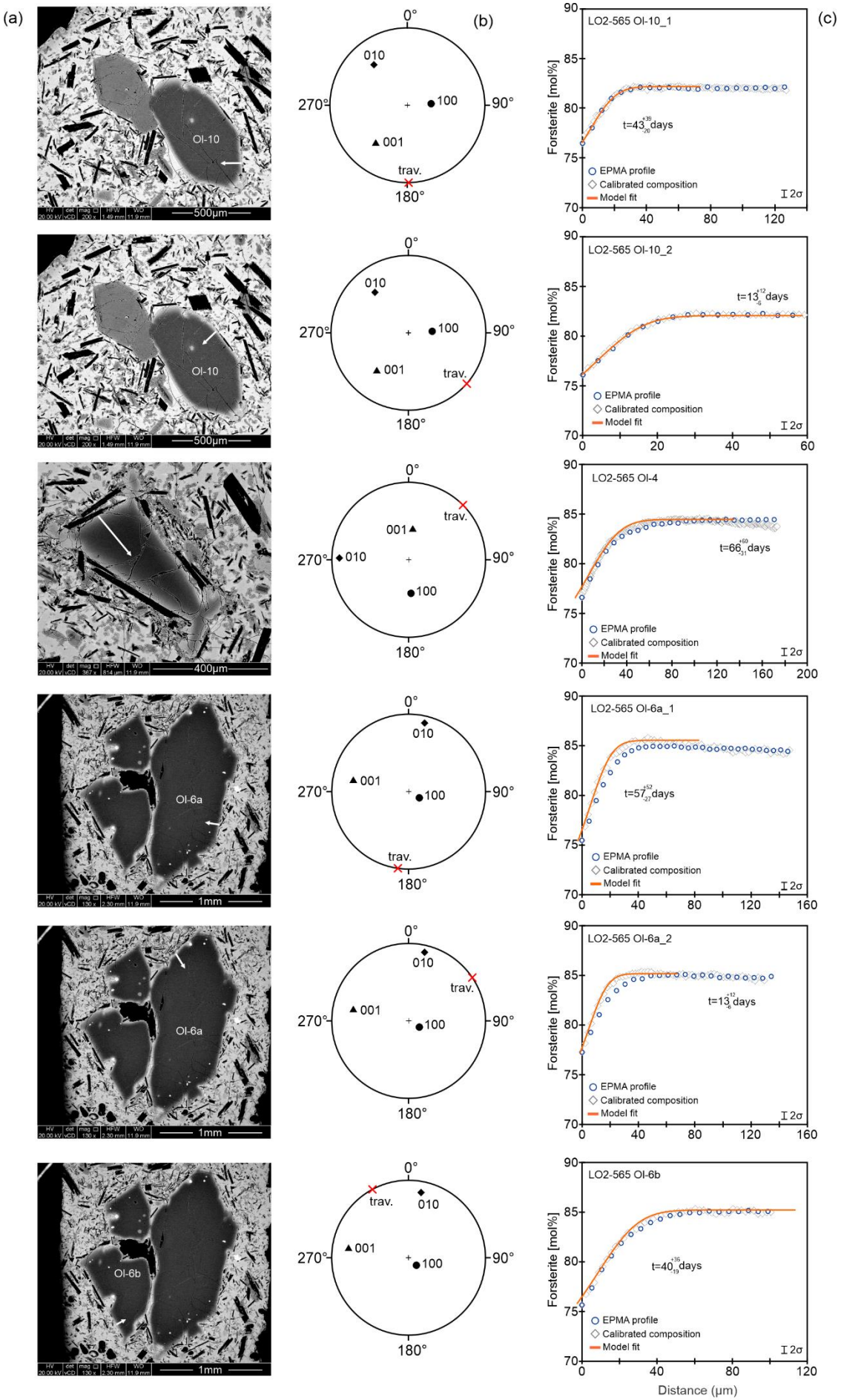

Supplementary Figure S27 - LO2-565

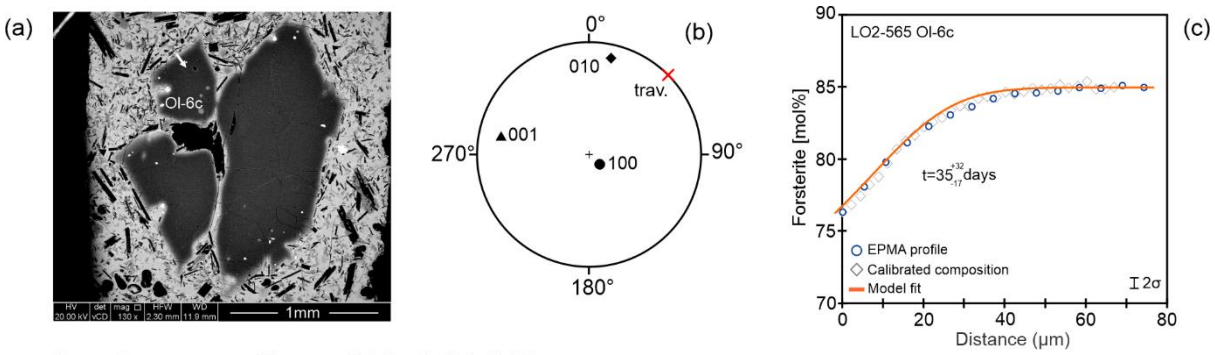

Supplementary Figure S28 - LO2-565

Supplementary Figures S9-S28. Data and best fit olivine diffusion models. (**A**) Backscattered electron (BSE) images of the analyzed olivine crystals. White arrows: Directions of EMP traverses. (**B**) Stereographic lower hemisphere plots depicting the angular relations between the main crystallographic axes in olivine and the directions of the analytical traverses (red x marked 'trav.'). (**C**) Rim to core concentration profiles of forsterite content. Orange and blue curves, best-fit diffusion models for the observed zoning profiles. Numbers in days indicate diffusive timescales obtained from best-fit model solutions. 1σ error bars refer to electron microprobe data.

REFERENCES

Ariskin AA, Frenkel MY, Barmina GS, and Nielsen RL (1993) COMAGMAT – A Fortran program to model magma differentiation processes: Computers and Geosciences Vol 19, pages 1166-1170. https://dx.doi.org/10.1016/0098-3004(93)90020-6

Armstrong JT (1988) Quantitative analysis of silicates and oxide minerals: comparison of Monte-Carlo, ZAF and Phi–Rho–Z procedures. In: Newbury DE (ed) Proceedings of the Microbeam Analysis Society, Microbeam Analysis Society, San Francisco: 239-246.

Armstrong JT (1991) Quantitative Elemental Analysis of Individual Microparticles with Electron Beam Instruments. In: Heinrich KFJ, Newbury DE (eds) Electron Probe Quantitation. Springer, Boston, MA. https://doi.org/10.1007/978-1-4899-2617-3_15

Armstrong JT (1993) Matrix correction program CITZAF, Version 3.5. California Institute of Technology.

Caracciolo A, Bali E, Guðfinnsson GH, Kahl M, Halldórsson SA, Hartley ME, Gunnarsson H (2020) Temporal evolution of magma and crystal mush storage conditions in the Bárðarbunga-Veiðivötn volcanic system, Iceland. Lithos 352-353. https://doi.org/10.1016/j.lithos.2019.105234

Clark AM, Long JVP (1971) The anisotropic diffusion of nickel in olivine. In: Sherwood, JN, Chadwick, AV, Muir, WM, Swinton, FL (eds) Diffusion Processes. Gordon & Breach: 511-521.

Costa F, Chakraborty S (2004) Decadal time gaps between mafic intrusion and silicic eruption obtained from chemical zoning patterns in olivine. Earth Planet Sci Lett 227: 517-530. https://doi.org/10.1016/j.epsl.2004.08.011

Couperthwaite FK, Morgan DJ, Harvey J, Kahl M (2022) Pre-eruptive timescales from the historical Hapaimamo eruption at Mauna Loa. J Volcanol Geotherm Res 432, 107690. https://doi.org/10.1016/j.jvolgeores.2022.107690

Couperthwaite FK, Morgan DJ, Pankhurst MJ, Lee PD, Day JMD (2021) Reducing epistemic and model uncertainty in ionic inter-diffusion chronology: a 3D observation and dynamic modeling approach using olivine from Piton de la Fournaise, La Réunion. Am Mineral 106: 481-494. https://doi.org/10.2138/am-2021-7296CCBY

Danyushevsky LV, Plechov P (2011) Petrolog3: Integrated software for modeling crystallization processes. Geochem Geophys Geosys 12:1-32. https://doi.org/10.1029/2011GC003516

Davis MG, Garcia MO, Wallace P (2003) Volatiles in glasses from Mauna Loa Volcano, Hawai‘i: implications for magma degassing and contamination, and growth of Hawaiian volcanoes. Cont Mineral Petrol 144: 570-591. https://doi.org/10.1007/s00410-002-0416-z

Dohmen R, Becker H-W, Chakraborty S (2007a) Fe–Mg diffusion in olivine I: experimental determination between 700 and 1,200°C as a function of composition, crystal orientation and oxygen fugacity. Phys Chem Mineral 34: 389-407. https://doi.org/10.1007/s00269-007-0157-7

Donovan J, Kremser D, Fournelle J (2012) Probe for EPMA: Acquisition, automation and analysis. Probe Software, Inc. (Eugene, Oregon).

Jarosewich E (2002) Smithsonian microbeam standards. Journal of Research of the National Institute of Standards and Technology 107: 681-685. doi: 10.6028/jres.107.054

Kahl M, Bali E, Guðfinnsson GH, Neave DA, Ubide T, van der Meer QHA, Matthews S (2021) Conditions and Dynamics of Magma Storage in the Snæfellsnes Volcanic Zone, Western Iceland: Insights from the Búðahraun and Berserkjahraun Eruptions. J Petrol 62: egab054. https://doi.org/10.1093/petrology/egab054

Kahl M, Viccaro M, Ubide T, Morgan DJ, Dingwell DB (2017) A branched magma feeder system during the 1669 eruption of Mt Etna: evidence from a time-integrated study of zoned olivine phenocryst populations. J Petrol 58: 443-472. doi:10.1093/petrology/egx022

Kress VC, Carmichael ISE (1988) Stoichiometry of the iron oxidation reaction in silicate melts. Am Mineral 73: 1267-1274.

Montierth C, Johnston AD, Cashman KV (1995) An empirical glass- composition-based geothermometer for Mauna Loa lavas. In: Rhodes, JM & Lockwood, JP (eds) Mauna Loa revealed: structure, composition, history, and hazards. AGU Monog 92: 207-217. https://doi.org/10.1029/GM092p0207

Mutch EJF, Maclennan J, Shorttle O, Rudge JF, Neave DA (2021) DFENS: Diffusion Chronometry Using Finite Elements and Nested Sampling. Geochem Geophys Geosys Vol 22., art no. e2020GC009303. https://dx.doi.org/10.1029/2020GC009303

Petrone C, Bugatti G, Braschi E., Tommasini S (2016) Pre-eruptive magmatic processes re-timed using a non-isothermal approach to magma chamber dynamics. Nature Communications 7: 12946. https://doi.org/10.1038/ncomms12946

Prior DJ, Boyle AP, Brenker F, Cheadle MC, Day A, Lopez G, Peruzzi L, Potts G, Reddy S, Spiess R, Timms NE (1999) The application of electron backscatter diffraction and orientation contrast imaging in the SEM to textural problems in rocks. Am Mineral 84: 1741-1759.

Putirka KD 2008 Thermometers and barometers for volcanic systems. Rev Mineral Geochem 69: 61-120. https://doi.org/10.2138/rmg.2008.69.3

Roeder PL, Emslie RF (1970) Olivine-liquid equilibrium. Cont Mineral Petrol 29: 275-289.

Rhodes JM (1988) Geochemistry of the 1984 Mauna Loa eruption: implications for magma storage and supply. J Geophys Res Solid Earth 93, B5: 4453-4466.

Shea T, Matzen AK, Mourey AJ (2022) Experimental study of Fe–Mg partitioning and zoning during rapid growth of olivine in Hawaiian tholeiites. Cont Mineral Petrol 177:114. https://doi.org/10.1007/s00410-022-01969-8

Thornber CR, Sherrod DR, Siems DF, Heliker CC, Meeker GP, Oscarson RL, Kauahikaua JP (2002) Whole-rock and glass major-element geochemistry of Kīlauea Volcano, Hawai‘i, near-vent eruptive products: September 1994 through September 2001. USGS Open File Rep 02-17: 41.

Thornber CR (2001) Olivine-liquid relations of lava erupted by Kīlauea volcano from 1994-1998: implications for shallow magmatic processes associated with the ongoing east rift zone eruption. Canadian Mineralogist 39: 239-266. https://doi.org/10.2113/gscanmin.39.2.239

Wieser PE, Kent AJR, Till CB, Donovan J, Neave DA, Blatter DL, Krawczynski MJ (2022) Barometers Behaving Badly I: Assessing the Influence of Analytical and Experimental Uncertainty on Clinopyroxene Thermobarometry Calculations at Crustal Conditions. Journal of Petrology 2023: 64, egac126. https://doi.org/10.1093/petrology/egac126